Facultad de Ciencias

ESTUDIO DEL DESLENSADO DEL MODO B DE POLARIZACIÓN DEL FONDO CÓSMICO DE MICROONDAS: DETECTABILIDAD DE LAS ONDAS GRAVITACIONALES PRIMORDIALES

On the Delensing of the Cosmic Microwave Background B-mode Polarization: Detectability of Primordial Gravitational Waves

Trabajo de Fin de Máster
para acceder al

MÁSTER INTERUNIVERSITARIO EN FÍSICA DE PARTÍCULAS Y DEL COSMOS

Autora: Patricia Diego Palazuelos

Director: Patricio Vielva Martínez

Septiembre 2019

Abstract

The most promising channel to detect the Primordial Gravitational Wave background, the smoking gun observable proving that an inflationary period took place, lies in the B-mode polarization of the Cosmic Microwave Background (CMB). However, due to its very low amplitude, the imprint it leaves on CMB polarization is vastly obscured by galactic microwave emissions and the B-mode polarization produced by weak gravitational lensing. As CMB experiments and component separation techniques are approaching the sensitivity at which lensed B-modes become the main obstacle in the detection of the primordial B-mode, we decided to study how well could the lensing effect be reversed for CMB maps with the noise levels that may be expected from future missions, and using high-quality reconstructions of the lensing potential. We found that lensing potential reconstructions must reach around a 500σ signal-to-noise ratio themselves to reduce the lensed B-mode spectrum to half its amplitude, conditions in which a 2σ detection of an $r = 6 \times 10^{-4}$ would be possible. For such reconstructions to be internally produced from the CMB, CMB maps must have an instrumental noise below the $1\mu K\cdot$ arcmin level.

KEYWORDS: Inflation, Gravitational Waves, Cosmic Microwave Background Polarization, Weak Gravitational Lensing

Resumen

El modo B de polarización del Fondo Cósmico de Microondas (FCM) constituye el canal más prometedor para la detección del fondo de Ondas Gravitacionales Primordiales, el observable que indiscutiblemente probaría la existencia de un periodo inflacionario. Sin embargo, debido a su extremadamente baja amplitud, la huella que deja en la polarización del FCM queda oculta muy por debajo la emisión en microondas de nuestra galaxia y del modo B inducido por el efecto lente gravitacional débil. Ahora que los experimentos del FCM y las técnicas de separación de componentes se están acercando a la sensibilidad a la cual los modos B lensados empieza a ser el principal obstáculo en la detección del modo B primordial, hemos decidido estudiar cómo de bien sería posible revertir el efecto lente en mapas del FCM con los niveles de ruido que cabría esperar de futuras misiones y usando reconstrucciones del potencial de lensing de alta calidad. Hemos encontrado que las reconstrucciones del potencial de lensing deben alcanzar un ratio señal-ruido de 500σ para conseguir reducir a la mitad la amplitud del modo B lensado, condiciones en las que una detección a 2σ de $r = 6 \times 10^{-4}$ sería posible. Si tales reconstrucciones han de producirse internamente a partir del FCM, los mapas del FCM deben contar con un ruido instrumental por debajo del nivel del $1\mu K\cdot$arcmin.

PALABRAS CLAVE: Inflación, Ondas Gravitacionales, Polarización del Fondo Cósmico de Microondas, Lente Gravitacional Débil

Foreword

The main goal of this project was to explore how well could it be possible to revert the effect that weak gravitational lensing has on the polarization of the Cosmic Microwave Background (CMB). This process, commonly known as *delensing*, is a crucial step in the search of the Primordial Gravitational Wave Background (PGWB) predicted by most inflationary models. We approached this problem by relying on numerical simulations, where we had full control over all the observables involved, to determine the quality of the CMB maps and lensing potential reconstructions that would be necessary to, after being delensed, allow the detection of the imprint that the PGWB leaves on the CMB polarization.

For this purpose, we decided to use some of the public codes developed by the CMB community. The lensing of the CMB was simulated using Antony Lewis' `LensPix`[1] code, while the discussion of the feasibility of CMB internal lensing potential reconstruction benefited from the use of Duncan Hanson's `quicklens`[2]. We also benefited from the access to the Altamira Supercomputer at the Institute of Physics of Cantabria (IFCA-CSIC), member of the Spanish Supercomputing Network, for performing our simulations and analysis. The author would also like to acknowledge that this research project was supported by a grant of the Spanish CSIC's JAE-Intro program.

Finally, this work is structured as follows. The first half of Chapter 1 offers an introduction to both, gravitational waves in general, and specially those produced in classical inflationary models. The mechanism through which this PGWB leads to the polarization of CMB photons, and how weak gravitational lensing obscures this polarization signal are explained in the second half of the chapter. The first section fo Chapter 2 is focused on the characterization of the simulations, while the rest of the chapter is dedicated to the description of the methodology adopted for the delensing process. The main results of our study on delensing efficiency and their implications for the detection of a primordial B-mode are presented in Chapter 3. In Chapter 4 we discuss the feasibility of achieving lensing potential reconstructions as good as the ones assumed here, and whether the results presented in the previous chapter are limited by the accuracy of the employed public code. Final conclusions and suggestions for future work are left for Chapter 5.

[1] https://cosmologist.info/lenspix/
[2] https://github.com/dhanson/quicklens

Index

CHAPTER 1

Introduction

In recent years, the direct detection of gravitational waves (GW) has become a common occurrence. Since the LIGO (Laser Interferometer Gravitational-Wave Observatory) Collaboration first announced the detection of the GW produced in the coalescence of two black holes back in 2016 [1], a total number of twelve GW events have been confirmed, and six months into their third observation run, now combining the Advanced LIGO and the European-based Virgo detectors, almost thirty possible events have already been detected [2]. Their success has definitely opened a new observation window into the universe.

Due to the frequency band at which they operate (approximately between 10 Hz to 10 kHz), ground interferometers like LIGO and Virgo are sensible to the GW produced in the final stages of orbiting compact binary systems before they merge [3]. In addition to these astrophysical sources, the existence of a cosmological background of GW is also predicted by the majority of inflationary models. These primordial gravitational waves (PGW) would be able to free-stream from times as early as (possibly) Planck scales, so they have the potential of becoming one of the most powerful cosmological probes, since they reach further into the history of the universe than other cosmological observables like the Cosmic Microwave Background (CMB) or the Large Scale Structure (LSS). Besides opening the possibility of new independent measurements of the cosmological parameters, and probing the properties of the potential driving inflation, the PGWB is also interesting for particle physicists, as its spectrum is sensitive to the phase transitions and particle creation/annihilation that took place in the early universe [4].

Having stated the physical interest and present-day relevance of the PGWB, the following sections are dedicated to exploring the GW background predicted by inflation and its connexion to the CMB science. Firstly, section 1.1 offers a brief introduction to the mathematical formalism of GW in the simple framework of *linearized gravity* in vacuum, while the actual production of GW in classical inflationary models and the properties of the predicted spectrum are tackled in section 1.2. As will be discussed in that section, the most promising approach to the detection of the PGWB is through the imprint it leaves in the polarization of the CMB. Therefore, section 1.3 will focus on how tensorial perturbations, like those produced by GW, can lead to the polarization of the CMB. Finally, section 1.4 is dedicated to introducing one of the main contaminants preventing us from detecting the signal left by PGW in the CMB polarization: the lensing CMB photons suffer as they pass through the LSS of the late universe. This constitutes the central point of this work, as we will try to determine how well can this effect be reverted.

1.1 Gravitational Waves on linearized gravity

In the framework of *linearized gravity*, as presented in reviews like [4] or [5], GW are introduced as a small perturbation $|h_{\mu\nu} << 1|$ over a flat Minkowski spacetime that leads to a perturbed metric

$$g_{\mu\nu}(x) = \eta_{\mu\nu}(x) + h_{\mu\nu}(x). \tag{1.1}$$

The $|h_{\mu\nu} << 1|$ condition effectively limits the perturbation to weak gravitational fields and restricts the set of coordinate systems where equation (1.1) holds.

To understand the effects and properties of GW, one should calculate the Einstein field equations $G_{\mu\nu} = \frac{8\pi G}{c^4} T_{\mu\nu}$ for that perturbed metric. Starting with the left-hand side of the equation, to construct the Einstein tensor the properties of the curvature of spacetime must be considered. To linear order in perturbation theory, the affine connection for the perturbed metric is

$$\Gamma^{\alpha}_{\mu\nu} \equiv \frac{1}{2} g^{\alpha\beta}(\partial_\nu g_{\beta\mu} + \partial_\mu g_{\alpha\nu} - \partial_\beta g_{\mu\nu}) = \frac{1}{2}(\partial_\nu h^{\alpha}_{\mu} + \partial_\mu h^{\alpha}_{\nu} - \partial^\alpha h_{\mu\nu}). \tag{1.2}$$

The Riemann tensor, which contains all the information about the curvature of spacetime, is computed from the affine connection like:

$$R^{\alpha}_{\mu\nu\beta} \equiv \partial_\nu \Gamma^{\alpha}_{\mu\beta} - \partial_\beta \Gamma^{\alpha}_{\mu\nu} = \frac{1}{2}(\partial_\mu \partial_\nu h^{\alpha}_{\beta} + \partial_\beta \partial^\alpha h_{\nu\mu} - \partial_\nu \partial^\alpha h_{\mu\beta} - \partial_\beta \partial_\mu h^{\alpha}_{\nu}). \tag{1.3}$$

Then, to compose the Einstein tensor, the information contained in the Riemann tensor has to be compacted into the Ricci tensor,

$$R_{\mu\nu} \equiv R^{\alpha}_{\mu\alpha\nu} = \frac{1}{2}(\partial_\nu \partial_\alpha h^{\alpha}_{\mu} + \partial_\mu \partial^\alpha h_{\nu\alpha} - \partial_\mu \partial_\nu h - \Box h_{\mu\nu}), \tag{1.4}$$

and the Ricci scalar,

$$R \equiv R^{\mu}_{\mu} = \partial^\alpha \partial_\beta h^{\beta}_{\alpha} - \Box h. \tag{1.5}$$

In these last two equations the d'Alembert operator $\Box \equiv \partial_\alpha \partial^\alpha = \nabla^2 - \partial_t^2$ has been introduced, and the notation for the perturbation's trace has been simplified to $h^{\alpha}_{\alpha} \equiv h$.

The Einstein tensor can be finally constructed from the Ricci tensor and scalar like:

$$G_{\mu\nu} \equiv R_{\mu\nu} - \frac{1}{2}\eta_{\mu\nu} R = \frac{1}{2}(\partial_\nu \partial_\alpha h^{\alpha}_{\mu} + \partial_\mu \partial^\alpha h_{\nu\alpha} - \partial_\mu \partial_\nu h - \Box h_{\mu\nu} - \eta_{\mu\nu} \partial^\alpha \partial_\beta h^{\beta}_{\alpha} + \eta_{\mu\nu} \Box h). \tag{1.6}$$

This expression can be simplified by using the *trace-reversed* formulation of the metric perturbation

$$\bar{h}_{\mu\nu} = h_{\mu\nu} - \frac{1}{2}\eta_{\mu\nu} h. \tag{1.7}$$

Due to this definition, the trace of $\bar{h}_{\mu\nu}$ has the opposite sign of that of $h_{\mu\nu}$ ($\bar{h} = -h$), hence earning the *trace-reversed* name. This change of sign has the effect of eliminating the trace terms when writing the Einstein tensor as a funciont of $\bar{h}_{\mu\nu}$:

$$G_{\mu\nu} = \frac{1}{2}(\partial_\nu \partial_\alpha \bar{h}^{\alpha}_{\mu} + \partial_\mu \partial^\alpha \bar{h}_{\nu\alpha} - \Box \bar{h}_{\mu\nu} - \eta_{\mu\nu} \partial^\alpha \partial_\beta \bar{h}^{\beta}_{\alpha}). \tag{1.8}$$

Notation. As is common practice in general relativity texts, Greek indices denote spacetime dimensions $\mu, \nu, \alpha... = 0, 1, 2, 3$, while Latin indices are reserved for spatial dimensions $i, j, k... = 1, 2, 3$. The Einstein convention is adopted, so that repeated indices should be interpreted as a sum over their values. We adopt the same signature for the Minkowski metric than our reference texts [4] and [5]: $\eta_{\mu\nu} \equiv diag(-1, +1, +1, +1)$.

With the Einstein tensor at hand, the field equations are then

$$\partial_\nu \partial_\alpha \bar{h}^\alpha_\mu + \partial_\mu \partial^\alpha \bar{h}_{\nu\alpha} - \Box \bar{h}_{\mu\nu} - \eta_{\mu\nu} \partial^\alpha \partial_\beta \bar{h}^\beta_\alpha = \frac{16\pi G}{c^4} T_{\mu\nu}. \tag{1.9}$$

However, it is very difficult to identify a propagating solution of the metric perturbation in this expression. To further simplify the field equations, an appropriate gauge that gets rid of all non-physical degrees of freedom must be chosen. The rightful choice for this case is the *Lorentz gauge*, where the metric perturbation verifies $\partial^\mu \bar{h}_{\mu\nu}(x) = 0$. In this gauge, equation (1.9) is then reduced to

$$\Box \bar{h}_{\mu\nu} = \frac{16\pi G}{c^4} T_{\mu\nu}, \tag{1.10}$$

which can be immediately recognized as a wave equation with a source term, where perturbations propagate at the speed of light.

Up to this point, we have demonstrated that indeed perturbations of spacetime do propagate as waves. However, the nature of such waves is still unknown. To determine their properties, we will have to consider the free propagation of GW in globally-vacuum flat spacetimes. By definition, a globally-vacuum flat spacetime is asymptotically flat, meaning that $h_{\mu\nu}(x) \to 0$ when $|x| \to \infty$, and verifies $T_{\mu\nu}(x) = 0$ at every point. In this scenario, the Lorentz gauge freedom can be further exploited.

As dicussed in [4], for a metric perturbation initially in the Lorentz gauge to stay in this family of gauges after a infinitesimal coordinate transformation $x'^\mu \to x^\mu + \xi^\mu$, the transformation vector ξ^μ has to satisfy

$$\Box \xi_\nu = \partial^\mu \bar{h}_{\mu\nu}(x) = 0. \tag{1.11}$$

The $\partial^\mu \bar{h}_{\mu\nu}(x) = 0$ condition imposes 4 constrains on $\bar{h}_{\mu\nu}$, reducing the initial 10 degrees of freedom contained in Einstein's field equations to 6. The second condition, $\Box \xi_\nu = 0$, entails another 4 constrains, therefore bringing the physical radiative degrees of freedom of GW down to only 2. However, since this last set of constraints does not explicitly act on $\bar{h}_{\mu\nu}$, this remaining gauge freedom can be used to directly eliminate some of the elements of the metric perturbation.

A particularly convenient specialization of the Lorentz gauge is that made in the *transverse-traceless* (TT) gauge, where the metric perturbation satifies

$$h_{\mu 0} = 0; \qquad h = h^i_i = 0; \qquad \partial_i h_{ij} = 0. \tag{1.12}$$

With these additional requirements, the local gauge freedom is completely fixed, ensuring that metric perturbations in the TT gauge contain only physical information and no gauge-artifacts. Recurring again to the Lorentz condition, the temporal components $h_{0\nu}$ can also be made zero, since $\partial^0 h_{0\nu} = 0$ means that they only involve the static part of the gravitational interaction (*i.e.*, the Newtonian potential) and GW are only concerned with the time-varying part of gravitation. Together, conditions $h_{\mu 0} = h_{0\nu} = 0$ make the perturbation purely spatial by removing all temporal components. The second condition ensures the metric perturbation is traceless, dismissing the necessity of differentiating between $\bar{h}_{\mu\nu}$ and $h_{\mu\nu}$ any more as they become equal. Another consequence of having a traceless perturbation is that the spatial distortions created by GW are area-conserving, since the determinant of the distortion remains unchanged. Finally,

the third condition implies that GW are transversal. This conclusion can be easily derived by applying the Lorenz gauge requierement of $\partial^\mu h_{\mu\nu} = 0$ to the plane wave expression of the metric perturbation $h_{\mu\nu}(x) = A_{\mu\nu}(k)e^{ik^\mu x_\mu}$, which gives $k^\mu h_{\mu\nu} = 0$. That equation restricts the spatial distortions created by the metric pertubation to lie in the plane perpendicular to the wave number vector k^μ, which indicates the propagation direction of the wave.

Under these conditions, a wave propagating in the $\vec{z}$ direction would take the form

$$h^{TT}_{\mu\nu}(x) = \begin{pmatrix} 0 & 0 & 0 & 0 \\ 0 & h_+ & h_\times & 0 \\ 0 & h_\times & -h_+ & 0 \\ 0 & 0 & 0 & 0 \end{pmatrix} e^{-i\omega t} e^{i(k_x x + k_y y)}, \tag{1.13}$$

where the only two independent components allowed by the TT gauge, h_+ and $h_\times$, correspond to the two possible polarization states GW can have. Writing down the perturbation the passing of this GW would produce in the line element,

$$ds^2 = -dt^2 + dz^2 + (1 + h_+)dx^2 + (1 - h_+)dy^2 + 2h_\times dxdy, \tag{1.14}$$

it is easy to see how the h_+ polarization state creates distortions along the $\vec{x}$ and $\vec{y}$ axes, while the $h_\times$ polarization state produces distortions along a 45° rotation of these axes (see Figure 1.1).

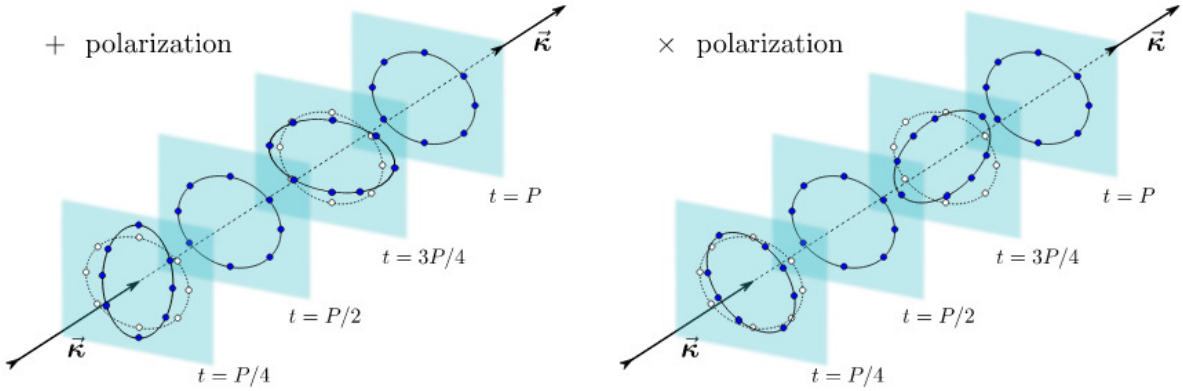

Figure 1.1: Spatial distortions created by the two possible polarization states of GW. The h_+ polarization state produces distortions along the $\vec{x}$ and $\vec{y}$ axes, while the ones produced by the $h_\times$ polarization are along a 45° rotation of these axes. Image taken from [6].

1.2 Generation of the PGWB during Inflation

Before inflation's proposal, the standard Big Bang paradigm could not satisfactory explain some of the experimental observations and, in particular, what is known as the *flatness* and *horizon problems* [7]. Measurements prove that the universe can be very well approximated by a flat Euclidean space [8], but for such level of flatness to be observed today an extreme fine-tuning of the early universe density is necessary. Moreover, at the time of the CMB's emission (approximately 380 000 years after the Big-Bang) only regions of the sky around one arc minute apart could have been causally connected, making hard to explain how regions outside this causal horizon had reached a level of homogeneity as great as that observed in the CMB.

The inflation mechanism was first proposed by Alan Guth in 1981 [9] as a dynamical solution to both the horizon and flatness problems. Inflation consists of a very short period ($\sim 10^{-34}$s) in the history of the early universe where it underwent an exponentially accelerated expansion, during which the scale parameter grew about ~ 27 orders of magnitude. Such tremendous expansion would have stretched space enough to make any initial curvature almost flat, granting the compatibility of today's flatness with all kind of initial conditions. This accelerated expansion is equivalent to a shrinking Hubble sphere, meaning that regions causally disconnected today were inside each other's particle horizons before inflation took place (see Figure 1.2), allowing communication and a thermal equilibrium between them. During inflation, these regions exit the horizon as the sudden expansion takes place, freezing the homogeneous density distribution across the sky. Only with time, detached regions become causally connected again as they reenter the horizon and start the process of gravitational collapse around small overdensities to form the structure observed today. Additionally, the inflation mechanism also explains why, even though particle physics models predict the existence of magnetic monopoles, none have been found. Any monopole density produced before or during inflation would have been diluted enough to become undetectable after such expansion.

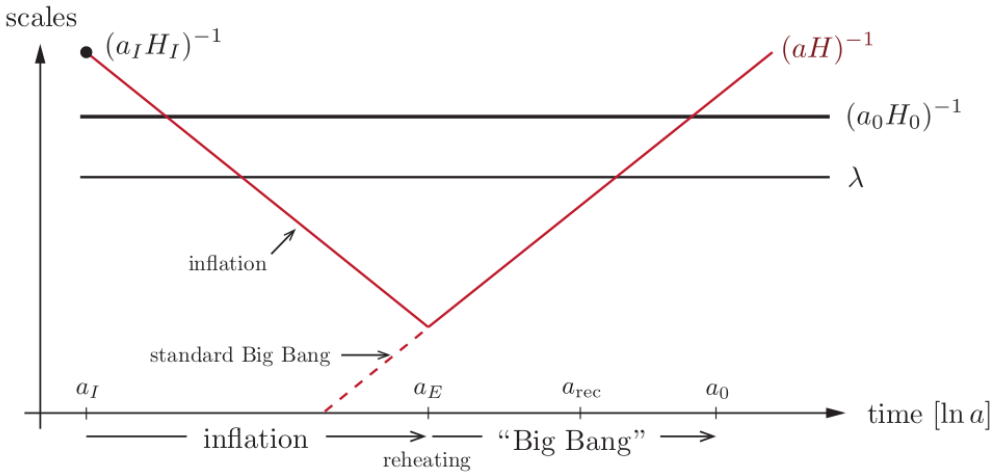

Figure 1.2: The causal history of the universe is dictated by the evolution of the *comoving Hubble radius* [1] $(aH)^{-1}$. At any given time, communication between sub-horizon scales ($\lambda < (aH)^{-1}$) is possible, while super-horizon scales ($\lambda > (aH)^{-1}$) are out of causal contact. In this way, inflation solves the horizon problem by introducing a period before the Big Bang where the Hubble radius decreases with time, allowing super-horizon scales at the time of CMB emission (a_{rec}) to have been in causal contact in the past. Image taken from [7].

But what drives the accelerated expansion? The physics of inflation is usually modeled by a scalar field, the *inflaton* $\psi(t, \vec{x})$, with a potential energy density $V(\psi)$ associated to each field value. If this field evolves with time, and the kinetic energy density it carries only makes a small contribution to the total energy, then its advance from a high energy state to a relaxed one can produce the accelerated expansion of inflation [10]. This scenario is known as *slow-roll inflation* (see Figure 1.3). Therefore, inflation ends when the potential steepens and the inflaton field picks up kinetic energy. Such energy, previously contained in the potential, is then transferred to Standard Model particles and starts the standard Big Bang in what is known as the *reheating* process.

[1] Properly speaking, causality is actually determined by the *particle horizon* χ_{ph}, which measures the maximum comoving distance that light can travel between two times. However, the comoving Hubble radius and the particle horizon are related:

$$\chi_{ph}(\tau) = \int_{t_I}^{t_0} \frac{dt}{a} = \int_{a_I}^{a_0} \frac{da}{a\dot{a}} = \int_{a_I}^{a_0} (aH)^{-1} d\ln a.$$

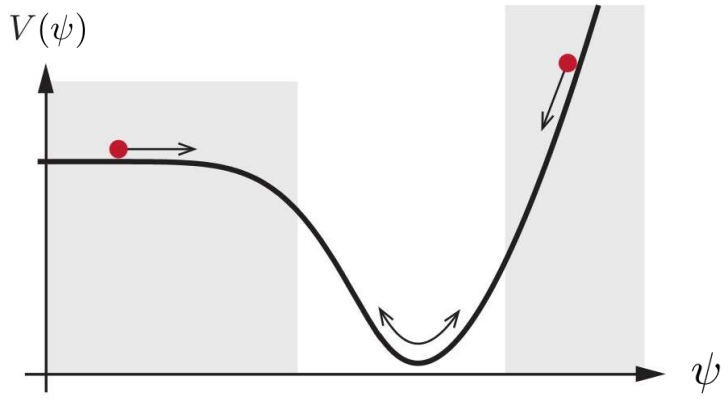

Figure 1.3: Example of a slow-roll potential. Inflation happens in the shaded areas of the potential, while reheating takes places when the field oscillates around the minimum of the potential. Image taken from [7].

Inflation is, therefore, a fundamental piece in our current understanding of the Standard Cosmological Model, and most of its predictions have already been experimentally proven (see Table 1.1). However, the observable considered by some to be the smoking gun proof that indeed an inflationary period existed, the stochastic Background of Primordial Gravitational Waves (PGWB), remains unobserved.

Inflation predicts ...	Current measurements prove
A spatially flat universe	$\Omega_k = 0.0007 \pm 0.0019$
with a nearly scale-invariant spectrum of density perturbations,	$n_s = 0.967 \pm 0.004$
that is almost a power law,	$dn/d\ln k = -0.0042 \pm 0.0067$
dominated by scalar perturbations,	$r_{0.002} < 0.07$
which are Gaussian	$f_{NL} = 2.5 \pm 5.7$
and adiabatic,	$\alpha_{-1} = 0.00013 \pm 0.00037$
with negligible topological defects.	$f < 0.01$

Table 1.1: Predictions the simplest inflationary models make on the curvature of space-time and on the nature of the matter distribution in the universe. All of them have been proved right by experimental measurements. Table taken from [8].

During inflation, any light field with a mass smaller than the Hubble rate $m^2 << H^2$ experiences quantum fluctuations [11, 12]. This includes tensor metric perturbations like the h_{ij} ones described in the previous sections since they correspond to massless fields. The exponential expansion of inflation then stretches the wavelength of this microscopic quantum fluctuations up to super-horizon scales. When they exit the horizon, the size of the fluctuations gets frozen and will not continue to evolve until they reenter the horizon at later times. Therefore, the earlier the fluctuations were generated, the greater the inflationary Hubble radius was at the time, and the bigger the angle they subtend in the sky would be now [4]. Besides, once they reenter the horizon, the amplitude of GW starts to decay as a^{-1}. Thus, GW that reentered the horizon in the matter-dominated era ($a \propto t^{2/3}$) would decay less than the ones that reentered during the radiation dominated era ($a \propto t^{1/2}$). From these two conditions, the PGW spectrum predicted by inflation is expected to reach its maximum amplitude at the smallest wavenumber (corresponding to the size of the horizon today) and to slowly decay towards lower scales (see Figure 1.4).

If detected, the PGWB would provide a lot of information about inflation [13]. The amplitude of the spectrum is directly related to the energy scale of inflation. The energy scale of reheating could also be measured from the highest frequency end of the spectrum (k_{rh} wavenumber associated to reheating) since it marks the beginning of the radiation dominated era. The lowest frequency mode observable today corresponds to the current horizon size, and the interval between the lowest frequency and k_{rh} would give

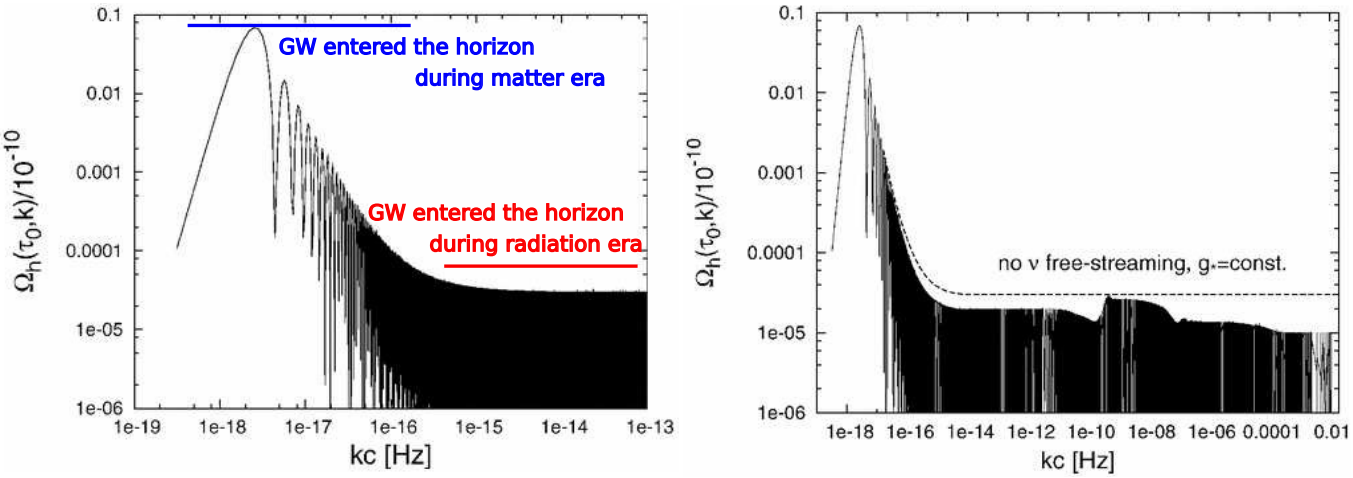

Figure 1.4: Relative spectral energy density of the PGWB at present day as a function of comoving wavenumber k (or kc in units of Hertz). The relative spectral energy density of PGW is computed from the PGW power spectrum like $\Omega_h(\tau_0,k) = \rho_h(\tau_0,k)/\rho_{cr}(\tau_0) = \mathcal{P}_h(\tau_0,k)[\mathcal{T}'(\tau_0,k)]^2/12a_0^2H_0^2$, where $\mathcal{T}'$ is the conformal time derivative of the *transfer function*, the function that dictates how the different scales reenter the horizon with time. Here the $\mathcal{P}_h$ was computed assuming a scale-invariant $n_T = 0$ primordial spectrum, an $\Omega_m = 1 - \Omega_r$, $\Omega_r = 4.15 \times 10^{-5}h^{-2}$, $h = 0.7$ cosmology, and $E_{inf} = 10^{16}$GeV. *Left panel:* Pure PGW spectrum. GW that reentered the horizon during the matter dominated era (smaller wavenumbers) decay less than the ones that reentered during the radiation dominated era (larger wavenumbers). *Right panel:* PGW spectrum after including the effects of the change in number of relativistic degrees of freedom during the radiation dominated era and neutrino free-streaming. Images adapted from [13].

the number of e-foldings, which determines the time elapsed between the end of inflation and the time when fluctuations that have the wavelength of the current horizon size left the horizon during inflation. The slope of the spectrum provides the power-law index of tensor perturbations n_T, which is predicted to be very small but different from zero, and its actual value would help to constrain inflationary models.

In addition, since PGW have been free-streaming since before reheating, their spectrum is sensitive to all the particle creations/annihilations that took place in the early universe. The change in the number of relativistic particles during the radiation dominated era affects the Hubble rate by reducing the growth rate of the Hubble radius during the transition [13]. Thus, the rate at which modes reenter the horizon is changed every time a Standard Model (or Beyond the Standard Model) particle stops being relativistic, leaving a characteristic step in the PGW spectrum at the frequency associated to the Hubble rate at the energy scale of the transition (see right panel of Figure 1.4).

However, given the current constraints CMB measurements impose on inflation, the amplitude of the PGW spectrum is expected to be so low that no current or near-future interferometer could directly detect it [3]. Luckily, as will be explained in the next section, tensorial perturbations produce the polarization of photons, and therefore, it should still be possible to indirectly detect the PGWB by the characteristic signal it leaves in the CMB polarization.

1.3 PGWB signature left in the CMB Polarization

The Cosmic Microwave Background (CMB) is a relic radiation coming from the *recombination time*, the period when the universe cooled enough to start forming neutral hydrogen atoms, thus freeing photons from the particle plasma for the first time [14]. Since up to that moment photons were in thermal equilibrium within the plasma, the CMB spectrum is a perfect blackbody reflecting the temperature of the universe at the time of photon decoupling $T_{rec} \sim 3100$K [7]. Emitted when the universe was around

380 000 years old ($z \sim 1100$), nowadays the spectrum is redshifted to $T = 2.7255 \pm 0.0006$K [15]. In addition, as photons were coupled to matter, the small matter overdensities that acted as the seeds of today's structure also created the small inhomogeneities of the order of $\sim 10^{-5}$K observed in the otherwise perfectly homogeneous and isotropic CMB radiation.

The existence of those small anisotropies guarantees that CMB radiation is also polarized [16]. During recombination, photons could still interact with not yet bound free electrons via Thomson scattering, an interaction that produces linearly polarized light in all but the incoming polarization direction [17]. In a purely isotropic photon bath, with photons of equal intensity coming from every direction, Thomson scattering with free electrons will produce unpolarized light. Only when the incoming intensity presents a quadrupole anisotropy, where the intensity coming from one direction surpasses the rest, the scattered radiation will be polarized (see Figure 1.5). In such a way, a quadrupole anisotropy around a scatterer electron will produce linearly polarized light in the direction of the cold axis.

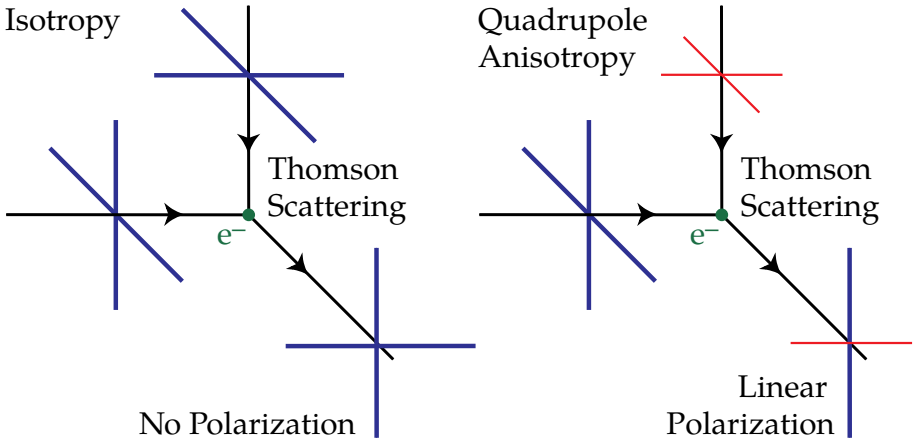

Figure 1.5: In a purely isotropic photon bath, with photons of equal intensity coming from every direction, Thomson scattering with free electrons will produce unpolarized light (left). Only when the incoming intensity presents a quadrupole anisotropy, where the intensity coming from one direction surpasses the rest, the scattered radiation will be polarized (right). Image adapted from [16].

Quantitatively, CMB radiation is commonly described in terms of the *Stokes parameters*, which, starting from a general monochromatic electromagnetic wave traveling along the $\vec{z}$ direction of components

$$E_x = a_x \cos(\omega t - \xi_x); \qquad E_y = a_y \sin(\omega t - \xi_y), \tag{1.15}$$

are defined like [17]:

$$I = a_x^2 + a_y^2; \;\; Q = a_x^2 - a_y^2; \;\; U = 2a_x a_y \cos(\xi_x - \xi_y); \;\; V = 2a_x a_y \sin(\xi_x - \xi_y). \tag{1.16}$$

The I parameter is simply the intensity, while Q and U respectively measure the degree of polarization along the $\vec{x}$ and $\vec{y}$ axis, and along a $45°$ rotation of them, and the V parameter describes circular polarization. Therefore, the I, Q and U parameters suffice to describe the linearly polarized light that conforms the CMB. An α rotation of the $\vec{x}$ and $\vec{y}$ axis produces a 2α rotation of the Q and U parameters, identifying them as the components of a spin-2 field. The proper way to express the polarization field on the surface of the sphere is then through the trace-free symmetric tensor [18]

$$P_{ab}(\vec{n}) = \frac{1}{2} \begin{pmatrix} Q(\vec{n}) & -U(\vec{n}) \sin\theta \\ -U(\vec{n}) \sin\theta & -Q(\vec{n}) \sin^2\theta \end{pmatrix}. \tag{1.17}$$

However, the definition of the Q and U parameters depends on the chosen coordinate system. Therefore, although they are the ones experimentally measured, a more convenient description of polarization independent of the choosing of coordinate system can be made in terms of the gradient and the curl of the polarization tensor:

$$\nabla^2 E = \partial_a \partial_b P_{ab}; \qquad \nabla^2 B = \epsilon_{ac} \partial_b \partial_c P_{ab}, \tag{1.18}$$

where ϵ_{ac} is the antisymmetric tensor

$$\epsilon_{ab} = \sqrt{g} \begin{pmatrix} 0 & 1 \\ -1 & 0 \end{pmatrix}. \tag{1.19}$$

Since they have a similar definition than that of the electric and magnetic components of electromagnetism, these new components are known as E- and B-modes. An example of how a polarization pattern expressed in terms of these E- and B-modes looks like is shown in Figure 1.6.

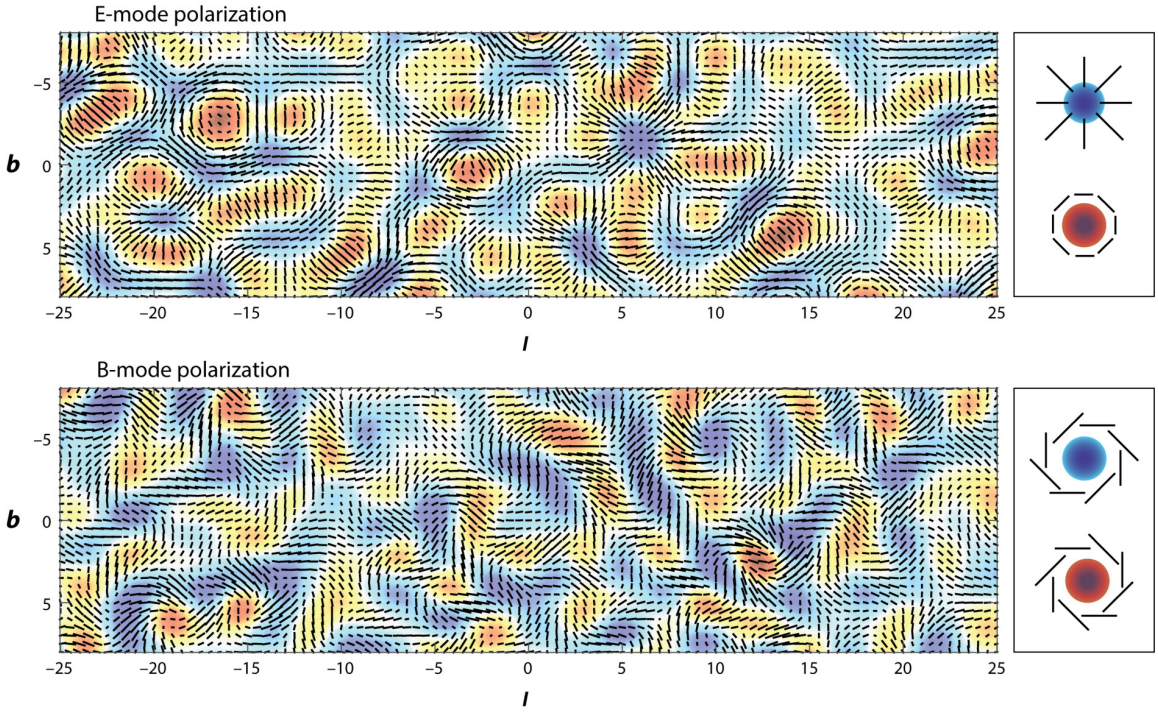

Figure 1.6: A polarization pattern composed only of E-modes (upper panel), and one composed only of B-modes (lower panel). As indicated on the right, the polarization patter of the E-mode is tangential around hot spots (red), and radial around cold spots (blue). In turn, the polarization pattern surrounding hot and cold spots of the B-mode shows a characteristic swirling with different orientations if it is a hot or cold spot. Image taken from [19].

But why should we look for PGW in the CMB polarization? To answer that question one must look at how the distribution of CMB photons evolves with time in the presence of GW. Initially, CMB photons have an homogeneous and isotropic unpolarized blackbody distribution

$$f = f_0(\nu) \begin{pmatrix} 1 \\ 1 \\ 0 \end{pmatrix} = \frac{1}{e^{h\nu/kT} - 1} \begin{pmatrix} 1 \\ 1 \\ 0 \end{pmatrix}. \tag{1.20}$$

Here, following the formalism of [20], radiation is described through the vector (I_θ, I_φ, U), which specifies the state of any radiation propagating in the $\vec{n} = (\theta, \varphi)$ direction with respect to the $\vec{\theta}$ and $\vec{\varphi}$ axes on the plane tangent to the sky at that point. The I and Q Stokes parameters are then calculated from the

vector components $I_\theta = a_\theta^2$ and $I_\varphi = a_\varphi^2$ like $I = I_\theta + I_\varphi$ and $Q = I_\theta - I_\varphi$. Therefore the distribution in (1.20) is indeed unpolarized. The time evolution of such photon distribution function is determined by the equation of radiative transfer (expressed in conformal time[2] η) [17]:

$$\frac{\partial f}{\partial \eta} + \vec{n}^i \frac{\partial f}{\partial x_i} = -\frac{d\nu}{d\eta}\frac{\partial f}{\partial \nu} - q(f - J). \tag{1.21}$$

The $q(f-J)$ term describes the effect of Thomson scattering, with $q = \sigma_T n_e a$ determining the scattering rate as a function of the Thomson cross-section σ_T, the number density of free-electrons n_e and the optical path a, and $J = J(\theta, \varphi, f)$ specifying how the initial intensity-polarization pattern is rearranged after being scattered. Meanwhile, the term $-\frac{d\nu}{d\eta}\frac{\partial f}{\partial \nu}$ reflects the gravitational redshift produced by the universe expansion.

The introduction now of a GW, of the h^+ polarization for example, would affect the frequency distribution of photons through the Sachs-Wolfe formula like [18, 21]

$$\frac{1}{\nu}\frac{d\nu}{d\eta} = \frac{1}{2}\frac{\partial h_{ij}^+}{\partial \eta}\vec{n}^i\vec{n}^j, \tag{1.22}$$

creating a perturbation in the initial distribution of photons

$$\tilde{f} = f_0(\nu)\left[\begin{pmatrix} 1 \\ 1 \\ 0 \end{pmatrix} + f_1\right]. \tag{1.23}$$

Attending to equation (1.22), the effect of a GW would be to generate an intensity pattern, that afterwards would produce a polarization pattern through Thomson scattering. Thefore, the f_1 perturbation must have to terms, a first one proportional to the original polarization, and a second one with the proper angular dependence dictated by J:

$$f_1 = \frac{\zeta}{2}(1-\mu^2)\cos 2\varphi \begin{pmatrix} 1 \\ 1 \\ 0 \end{pmatrix} + \frac{\beta}{2}\begin{pmatrix} (1+\mu^2)\cos 2\varphi \\ -(1+\mu^2)\cos 2\varphi \\ 4\mu \sin 2\varphi \end{pmatrix}, \tag{1.24}$$

where $\mu = \cos\theta$, and the ζ and β coefficients respectively specify the intensity and polarization anisotropy produced by the GW. Those coefficients must be determined by solving the radiative transfer equation. Finally, retaining only the linear terms in the h^+ perturbation after taking the Fourier transform of (1.21) and integrating over $d\mu$ [21], the following set of coupled differential equations is obtained:

$$\begin{aligned} \dot{\xi}_k + [ik\mu + q]\xi_k &= \dot{h}_k^+ \frac{d\ln f_0}{d\ln \nu_0}; \\ \dot{\beta}_k + [ik\mu + q]\beta_k &= \frac{3}{16}q\int d\mu' \Big[(1+\mu'^2)^2\beta_k - \frac{1}{2}(1-\mu'^2)^2\xi_k\Big], \end{aligned} \tag{1.25}$$

where $\xi_k = \zeta_k + \beta_k$, k is the wavenumber, and $\dot{x}$ means conformal time derivative. Again it can be seen how in the first equation an intensity anisotry is produced from the GW, while in the second one polarization is generated through the scattering of that intensity fluctuation. In practice, these equations are commonly expanded in terms of Legendre polynomials and numerically solved by propagating the known solution from some very early time where it can be analytically determined.

[2] Conformal time is defined as $\eta = \int dt/a(t)$.

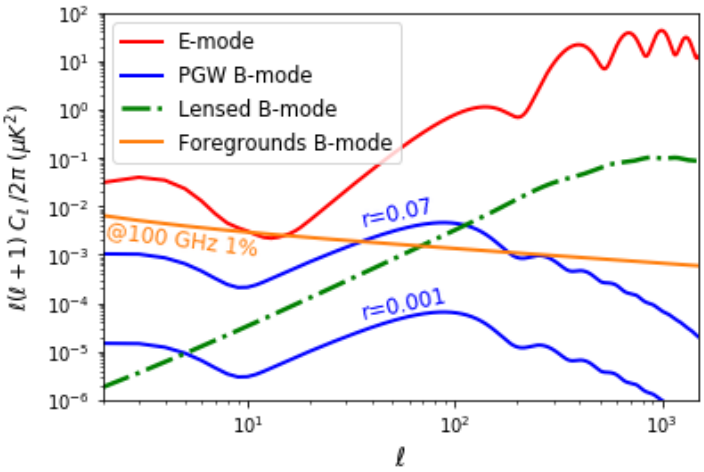

Figure 1.7: Angular power spectrum of the total E- (red) and B-mode (blue) CMB polarization when considering the polarization component generated by a PGW spectrum of amplitude $r = 0.07$ (current upper limit set by the *Planck* mission [8]) and $r = 0.001$. The scalar B-modes produced by weak gravitational lensing (green dot-dashed line) and the galactic foreground B-mode spectrum expected for the cleanest 1% of the sky at 100GHz (orange solid line) are also included to illustrate the difficulties faced int the detection of the primordial B-mode spectrum.

Figure 1.7 shows the angular power spectra of the E- and B-mode CMB polarization generated when introducing the PGW spectrum $\mathcal{P}_h(k)$ in equations (1.25). Two different amplitudes of the PGW are assumed, represented by the choice of tensor-to-scalar ratio $r = \mathcal{P}_h(k)/\mathcal{P}_s(k)$, *i.e.*, the ratio between tensor and scalar perturbations. Although the contribution of PGW to the E-mode spectrum is minimal, being more than two orders of magnitude lower than the intrinsic component, it is the only source of B-mode polarization since the CMB does not have an intrinsic B-mode spectrum. In addition, while tensor perturbations (like the ones produced by GW) generate both E- and B-modes, scalar perturbations (like the ones that produced the density inhomogeneities that led to today's structure) can only generate E-mode polarization due to their parity [22]. Therefore, B-mode polarization constitutes the optimal channel for PGW detection.

However, as can be seen in Figure 1.7, the primordial B-mode signal is vastly obscured by that of galactic microwave emissions and the scalar B-modes produced by weak gravitational lensing. Inside our galaxy, polarized microwave radiation is mainly produced by synchrotron radiation and thermal dust emission [23]. Such microwave emissions, usually known as *foregrounds* in the context of the CMB since strictly they were emitted much later, are the main contaminant obstructing the detection of a primordial B-mode [24,25]. Furthermore, the weak gravitational lensing of CMB photons produced by the large-scale structure present in the late universe generates the transfer of E-modes into an additional scalar B-mode component. Removing this lensing signal is precisely the main objective of this work.

1.4 Lensing of the CMB

As mentioned before, in their way to us CMB photons are subject to the gravitational lensing effect exerted by the large-scale structure of the universe, hence making the observed CMB a lensed version of the original one. The weak lensing regime is enough to describe the deflection experimented by photons as they traverse the various under- and over-densities, since the total expected deflection is of about ~ 2 arcmin given the characteristic depth and size of the potential wells and the distance traveled. However, deflection angles will be correlated over the sky by the angle given by the angular size of potential wells,

which can be of about $\sim 2^\circ$ for a potential midway to last scattering. Therefore, although deflections are small, lensing has an observable effect at the scale of the primary acoustic peaks.

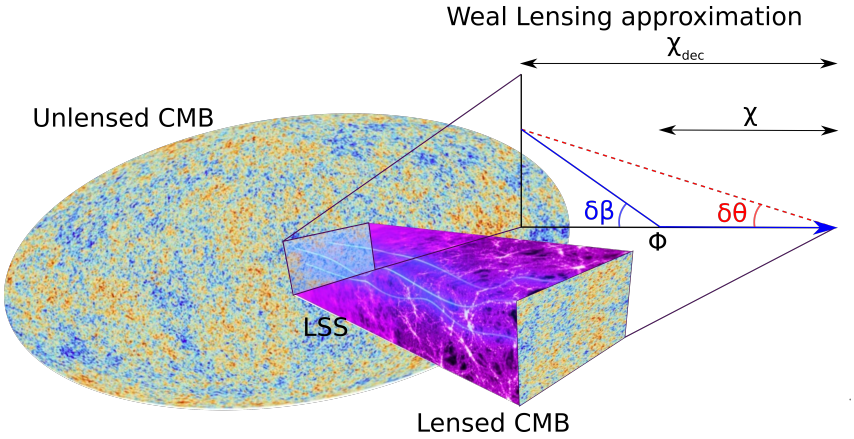

Figure 1.8: In their way to us CMB photons are deflected as they traverse the various under- and over-densities of the large-scale structure of the universe, hence making the observed CMB a lensed version of the original one. Since deflections are expected to be small, of the order of ~ 2 arcmin, the weak lensing regime is enough to describe the lensing of CMB photons.

To quantitatively determine the total deflection angle $\vec{\alpha}$, one must resort to General Relativity. As is thoroughly explained in [26], photons traveling near a mass distribution will expermient a tranversal acceleration given by the gradient of the gravitational potential Φ. The effect of such acceleration is to produce a local deflection angle of $\delta\beta = -2\delta\chi\nabla_\perp\Phi$, where $\delta\chi$ is a small distance along the photon path, that for the observer would be seen as a $\delta\theta$ change in the observed angle. The comoving distance that the light would appear to have moved due to lensing is then, in the small angle approximation, $f_K(\chi_{dec}-\chi)\delta\beta = f_K(\chi_{dec})\delta\theta$ (see Figure 1.8), where $f_K(\chi)$ is the *angular diameter distance*, the function that relates comoving distances to angles depending on the curvature of space:

$$f_K(\chi) = \begin{cases} K^{-1/2}\sin(K^{1/2}\chi) & K>0, \text{closed} \\ \chi & K=0, \text{flat} \\ |K|^{-1/2}\sinh(|K|^{1/2}\chi) & K<0, \text{open} \end{cases} . \tag{1.26}$$

Solving for $\delta\theta$, the deflection due to a potential well at comoving distance χ will be

$$\delta\theta = \frac{f_K(\chi_{dec}-\chi)}{f_K(\chi_{dec})}\delta\beta = -2\frac{f_K(\chi_{dec}-\chi)}{f_K(\chi_{dec})}\delta\chi\nabla_\perp\Phi \tag{1.27}$$

in the direction of $\nabla_\perp\Phi$. Integrating up the deflections from all the potential gradients between us and the time when the CMB was emitted at χ_{dec}, the total deflection angle is:

$$\vec{\alpha} = -2\int_0^{\chi_{dec}} d\chi \frac{f_K(\chi_{dec}-\chi)}{f_K(\chi_{dec})}\nabla_\perp\Phi(\chi\vec{n}, \eta_0-\chi). \tag{1.28}$$

To account for the time evolution of potential wells, the gradient of the potential is evaluated at the conformal time $\eta_0-\chi$ when the photon was at position $\chi\vec{n}$. This expression is only valid in the weak lensing regime (*i.e.*, small deflection angles) and is only accurate to lowest order in the potential.

The calculation of the deflection angle can be simplified by defining an effective integrated potential, the *lensing potential*. The tranverse component of the gradient in equation (1.28) can be rewritten as $\nabla_\perp\Phi = \nabla_{\vec{n}}\Phi/f_K(\chi)$, where $\nabla_{\vec{n}}$ represent the angular derivative, which is equivalent to the covariant

derivative on the sphere at $\vec{n}$. Therefore, from now on we may simply write it as ∇. In this way, equation (1.28) adopts the form

$$\vec{\alpha} = -2 \int_0^{\chi_{dec}} d\chi \frac{f_K(\chi_{dec} - \chi)}{f_K(\chi_{dec}) f_K(\chi)} \nabla \Phi(\chi \vec{n}, \eta_0 - \chi), \tag{1.29}$$

and the lensing potential is defined by taking the derivative out of the integral like

$$\phi(\vec{n}) \equiv -2 \int_0^{\chi_{dec}} d\chi \frac{f_K(\chi_{dec} - \chi)}{f_K(\chi_{dec}) f_K(\chi)} \Phi(\chi \vec{n}, \eta_0 - \chi) \tag{1.30}$$

so that the deflection angle is simply calculated by $\vec{\alpha} = \nabla \phi(\vec{n})$. In this way, if recombination is approximated to be an instantaneous process so that the CMB is emitted in a single source plane at $\chi = \chi_{dec}$, and the very small effect of late-time sources and reionization is neglected, all the information required for lensing can be contained in a simple 2D map of the lensing potential on the sphere. As an example, Figure 1.9 shows the best estimate of the lensing deflection angle map $\alpha(\vec{n})$ obtained by the Planck Collaboration [27], and the expected angular power spectrum of the lensing potential.

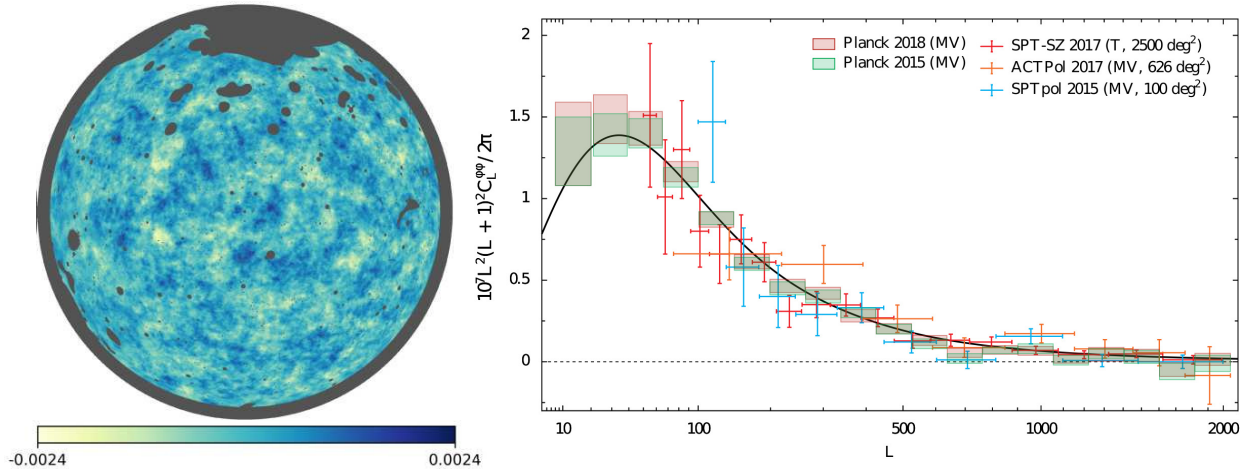

Figure 1.9: *Left panel:* Lensing deflection angle $\alpha(\vec{n})$ reconstructed from a combination of the minimum variance quadratic estimator and the Cosmic Infrarred Background by the Planck Collaboration [27]. The map shows the orthographic projection centered at the south Galactic pole, including in gray some masked regions. *Right panel:* Power spectrum of the lensing potential according to the *Planck* baseline model published in the full-mission final release [28] (black line), along with different recent measurements made by several collaborations. Image taken from [27].

But what effects does lensing have on the observed CMB? Lensing by transverse gradients does not change the frequency distribution of photons. Therefore, the lensed CMB has the same blackbody spectrum than the unlensed CMB. It is only due to secondary processes like the Sunyaev-Zel'dovich effect, where CMB photons interact through inverse Compton scattering with the high-energy electrons present in galaxy clusters, that the CMB blackbody spectrum gets distorted. The number of photons per solid angle remains the same too since lensing conserves surface brightness, because although the lensing induced magnification does increase the number of photons received from a certain patch, the angular size subtented by that patch also increases proportionaly. In this way, the lensing of a perfectly isotropic CMB will be undetectable, as photons would be simply moved around but arrive in the same distribution as before, and is only thanks to the presence of anisotropies that lensing is an observable effect.

At the power spectrum level, the effect lensing has over the unlensed temperature and E-mode polarization spectra is [29]:

$$\tilde{C}_\ell^{TT} = \left(1 - \ell^2 R^\phi\right) C_\ell^{TT} + \int \frac{d^2 l'}{(2\pi)^2} [l' \cdot (l - l')]^2 C_{|l-l'|}^{\phi\phi} C_{\ell'}^{TT} \tag{1.31}$$

$$\tilde{C}_\ell^{EE} = \left(1 - \ell^2 R^\phi\right) C_\ell^{EE} + \int \frac{d^2 l'}{(2\pi)^2} [l' \cdot (l - l')]^2 C_{|l-l'|}^{\phi\phi} C_{|l'|}^{EE} \cos^2 2(\varphi_{l'} - \varphi_l) \tag{1.32}$$

where l indicates a point in harmonic space $l = (\ell, m)$ and the $\cos^2 2(\varphi_{l'} - \varphi_l)$ term is the rotation of the l' base in the direction of l. The second term on the right-hand side of these equations is a convolution in harmonic space, and R^ϕ is half the total deflection angle power

$$R^\phi = \frac{1}{2} \langle |\nabla \phi| \rangle^2 = \frac{1}{4\pi} \int \frac{d\ell}{\ell} \ell^4 C_\ell^{\phi\phi}. \tag{1.33}$$

Since $\ell^4 C_\ell^{\phi\phi}$ has so little power (see Figure 1.9), its contribution can be neglected in a first approximation. Thus, lensing can essentially be understood as a convolution between the CMB spectra and the lensing potential, which main effect is to smooth out the acoustic peaks (see Figure 1.10). Given the correlation that exists between temperature and E-mode polarization, this dampening effect also propagates to the cross-spectrum C_ℓ^{TE}.

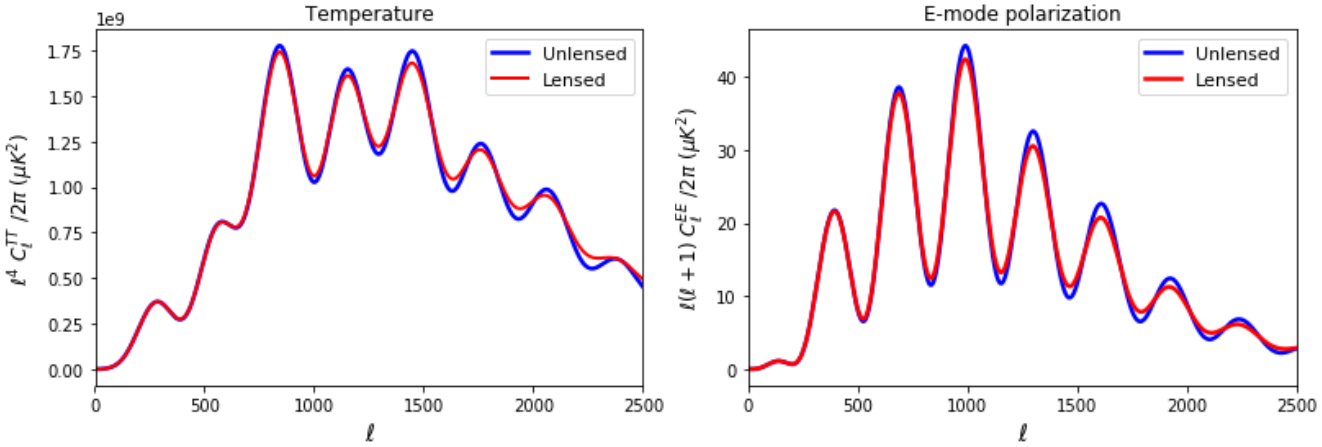

Figure 1.10: Comparison between the lensed and unlensed temperature (left) and E-mode polarization (right) power spectra. Note the use of the l^4 factor multiplying the C_ℓ^{TT} spectrum rather than the common $\sim l^2$ one to amplify the smallest scales and make visible the damping effect lensing has on the acoustic peaks.

In turn, even when no primordial B-mode is assumed, lensing will generate B-mode polarization from the E-mode

$$\tilde{C}_\ell^{BB} = \int \frac{d^2 l'}{(2\pi)^2} [l' \cdot (l - l')]^2 C_{|l-l'|}^{\phi\phi} C_{|l'|}^{EE} \sin^2 2(\varphi_{l'} - \varphi_l), \tag{1.34}$$

producing a scalar B-mode component like the one shown in Figure 1.7. The spectrum of this lensed B-modes is nearly constant on the largest scales, behaving effectively like white noise up to $\ell \sim 1000$, and difficulting the detection of any primordial B-mode.

In terms of other CMB statistics, lensing is also a source of non-Gaussianity [26], since it is a non-linear operation between two nearly Gaussian fields, the unlensed CMB and the lensing potential. Therefore, the lensed CMB has a non-zero bispectrum (or three-point correlation function), which can be used as a probe of perturbation growth and the expansion history at low redshift, and a non-zero trispectrum (or four-point correlation function), that can be used to reconstruct the lensing potential.

CHAPTER 2

Delensing methodology

2.1 Characterization of the work simulations

Acknowledging that our results will be constrained by the precision in the reproduction of the lensing effect, a detailed characterization of the work simulations must be done before proposing any delensing method. For our simulations we chose to rely on some of the public codes already developed by the CMB community. Theoretical power spectra were numerically computed using `CAMB`[1], by Antony Lewis and Anthony Challinor, while the lensing of the CMB was simulated with `LensPix`, a `Fortran` code developed by Antony Lewis. The cosmological model assumed in all the simulations is the 2018 full-mission final *Planck* baseline model [28].

Firstly, a bit of insight into how the code works is needed. `LensPix` recreates the lensing of CMB fields through pixel remapping [30]. As they pass through the LSS present in the late universe, CMB photons coming from an original direction $\vec{n}'$ get deflected to a new direction $\vec{n}$. Thus, an observed lensed CMB field $\tilde{X}(\vec{n})$ is just a remapped version of the original field $X(\vec{n}')$:

$$\tilde{X}(\vec{n}) = X(\vec{n}') = X(\vec{n} + \nabla\phi(\vec{n})), \tag{2.1}$$

where X stands for both temperature and polarization maps $X = T, Q, U$. In this remapping $\vec{n}' = \vec{n} + \nabla\phi(\vec{n})$, and the original direction $\vec{n}'$ can be obtained from the observed direction $\vec{n}$ by moving its end on the surface of the sphere a distance $|\nabla\phi(\vec{n})|$ along the geodesic in the direction of $\nabla\phi(\vec{n})$. Remember that in this expressions the ∇ operator means covariant derivative in the sphere. `LensPix` works in the *Born approximation* [26], where deflections can be calculated through lensing potential gradients along the undeflected path, so that $|\nabla\phi|$ can be assumed to be constant between $\vec{n}$ and $\vec{n}'$. The implementation of this remapping is quite straightforward for temperature maps, but more complicated for polarization, since one has to ensure the parallel transport of vector quantities along the geodesics.

Given that the typical lensing deflection is of about $\sim 2'$, high-resolution maps are necessary to properly reproduce this point to point remapping. In the `HEALPix` pixelization (the canonical pixelization of the sphere used in CMB science [31]) around $\sim 12.6 \times 10^6$ pixels are needed to achieve a $3.43'$ resolution. This means that every realization of a temperature and polarization pair of CMB maps will weight 145MB, plus the additional 49MB of the lensing potential. The need for extense computational resources becomes

[1] https://camb.info/

obvious in light of the volume of data involved, especially when one aims to make enough lensed and delensed versions of these maps to statistically characterize them, and repeat the process for different noises and lensing potentials. This is why we resorted to the Altamira Supercomputer[2] to execute our calculations. Even then, the remapping of such volume of pixels still required 22 minutes of computational time when using 16 cores. Nonetheless, a $3.43'$ resolution ($\mathrm{nside} = 1024$) proved to be the optimal for our purposes, since remapping could not accurately reproduce lensing for lowers resolutions, and an upgrade to a $1.8'$ resolution only resulted in an increase of the computational time and storage space required without a significant improvement in the accuracy of the lensing reproduction at the multipole range of interest.

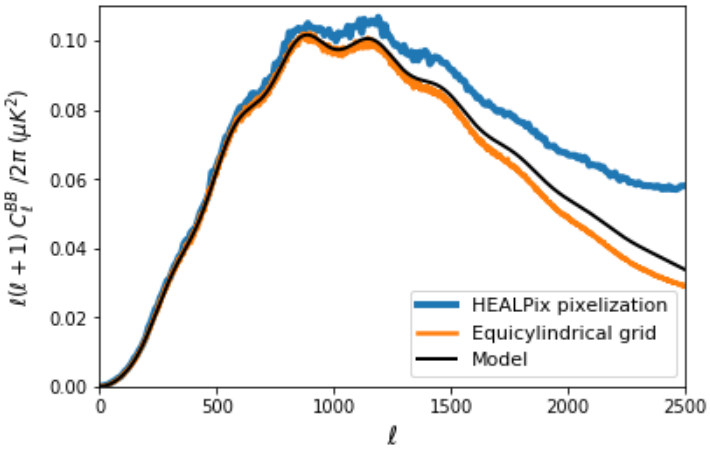

Figure 2.1: For the same resolution, the equicylindrical grid interpolation reproduces much better the model B-mode polarization than the naive `HEALPix` remapping.

For its remapping, `LensPix` offers two interpolation mechanisms: a naive remapping using the `HEALPix` pixelization of the sphere, and a more precise cubic interpolation using a high-resolution equicylindrical grid [32]. A quick test demonstrated that, when it comes to the reproduction of lensed B-modes, the latter interpolation method gives indeed much more accurate results (see Figure 2.1). Besides, due to the way the number of pixels is scaled when the map resolution increases, the `HEALPix` remapping takes about four times the computational time needed for the equicylindrical grid interpolation to produce lensed maps of the same resolution. Therefore, we adopted the equicylindrical grid interpolation method for all of our simulations.

Figure 2.2 shows the temperature and E-mode polarization lensed spectra obtained this way. In these graphs one can see how the `LensPix` simulated C_ℓ^{TT} and C_ℓ^{EE} lensed spectra follow the expected model, dampening the peaks of the small scale oscillations. However, when comparing with the B-mode spectrum of Figure 2.1, it is evident how the C_ℓ^{BB} spectrum starts to deviate from the model at a much lower multipole than the other two.

In its website[3], `LensPix` is said to achieve a $\sim 0.1\%$ accuracy in the reproduction of lensed temperature and E-mode polarization power spectra for multipoles $\ell < 2000$. No accuracy is specified for B-mode polarization, merely alerting that errors are much larger in this case. In order to verify this statement, and

[2] https://confluence.ifca.es/display/IC/High+Performance+Computing
[3] https://cosmologist.info/lenspix/

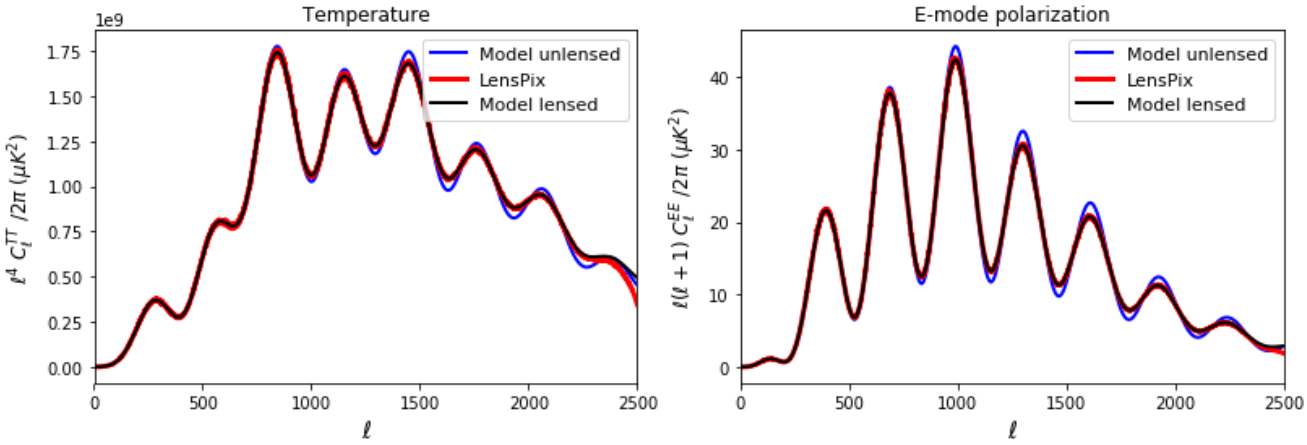

Figure 2.2: Comparison between the temperature and E-mode polarization power spectra simulated with `LensPix` and the theoretical lensed and unlensed ones calculated with `CAMB`. Up to the accuracy of `LensPix` calculations, its spectra clearly obeys to the lensed model rather than the unlensed prediction.

to estimate the accuracy in the reproduction of the lensed B-mode spectrum, we calculated the percentage error $[1-(C^{XX}_{\ell,\mathrm{LensPix}}/C^{XX}_{\ell,\mathrm{Model}})]\times 100$ by which `LensPix`'s simulations deviate from the `CAMB` spectra. The `LensPix` spectra used for this calculation were obtained by averaging over twenty five simulations. As can be seen in Figure 2.3, C_ℓ^{TT} and C_ℓ^{EE} meet the reported precision, while the C_ℓ^{BB} error starts to grow well above percentage level for $\ell > 1000$. This distinct behavior in the accuracy of the reproduction of B-mode polarization showcases some of the limitations of the `LensPix` code and will be a topic for later discussion. For now, we will limit our analysis and results to multipoles $\ell < 1000$, where a mean $\sim 0.2\%$ accuracy can be guaranteed for B-modes. As a quick reference for the interpretation of future plots, $\ell = 1000$ lies just after the maximum in the lensed B-mode spectrum.

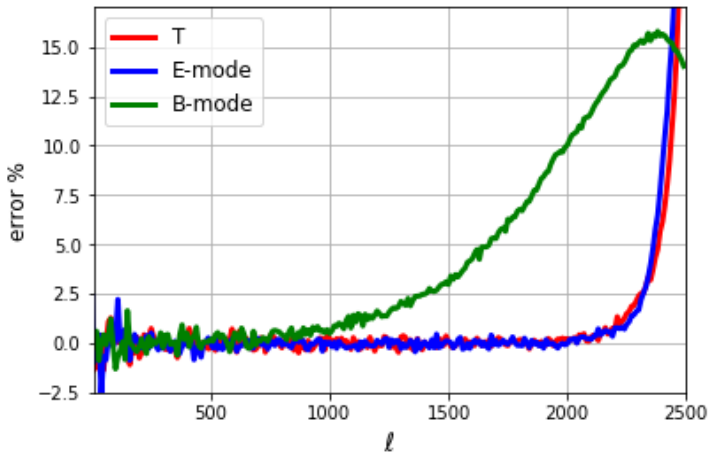

Figure 2.3: `LensPix` accuracy to reproduce the lensing of CMB temperature and polarization maps represented as the percentage error $[1-(C^{XX}_{\ell,\mathrm{LensPix}}/C^{XX}_{\ell,\mathrm{Model}})]\times 100$ between the `CAMB` model and `LensPix`'s simulations. To compute these errors, `LensPix` C_ℓs were averaged over twenty five simulations of the same cosmological model.

2.2 Antilensing approximation and pipeline description

The main ingredient needed to revert the small deviations that weak gravitational lensing induces on CMB photons is precisely the lensing potential that caused such deviations. Therefore, most of the efforts collected in the literature are focused on how to estimate this lensing potential. Estimates of the lensing potential can be reconstructed from the lensed CMB itself [33], or through other tracers of the

large-scale structure of the universe [34]. Accordingly, in order to reproduce these real-life scenarios where delensing has to be done with imperfect reconstructions of the lensing potential, we must add some instrumental noise and degrade the resolution of the initial lensing potential produced by our simulations. The CMB maps to delens will also be degraded to reproduce some of the typical instrumental resolutions and noise sensitivities that could be expected from future experiments. The description and justification of the choice of noise levels and resolutions for these degraded maps are left to section 2.3.

Under these conditions, and remembering how `LensPix` reproduces the lensing of CMB photons, the most straightforward approach to revert the displacements produced by weak gravitational lensing would be to just lens the already lensed map with the opposite lensing potential, effectively remapping each pixel to its original position. Although intuitive, this delensing strategy (dubbed as *antilensing* in the bibliography [35]) is in fact only an approximate solution. To clarify where the approximation fails, let us rewrite the relation between the lensed and unlensed maps like

$$\tilde{X}(\vec{n}) = X(f(\vec{n})); \qquad X(\vec{n}) = \tilde{X}(g(\vec{n})), \tag{2.2}$$

where the remapping function $f(\vec{n})$ is defined as $f(\vec{n}) \equiv \vec{n} + \nabla\phi(\vec{n})$. Likewise, the inverse remapping should consist on another displacement $d(\vec{n})$ such that $g(\vec{n}) \equiv \vec{n} + d(\vec{n})$. The expression for this inverse displacement $d(\vec{n})$ can be found by requiring the inverse remapping to verify $g(f(\vec{n})) = \vec{n}$. That condition implies that

$$d(f(\vec{n})) = -\nabla\phi(\vec{n}), \tag{2.3}$$

and therefore, the inverse displacement must be computed from the lensed map like

$$d(\vec{n}) = -\nabla\phi(g(\vec{n})) = -\nabla\phi(\vec{n} + d(\vec{n})). \tag{2.4}$$

Hence, an exact delensing method would require the numerical resolution of equation (2.4) at every point in order to remap pixels back to their unlensed positions [33]. Let me remark that because of this definition, the inverse displacement always has a small curl component, even in the case where the forward displacement $\nabla\phi$ is a pure gradient.

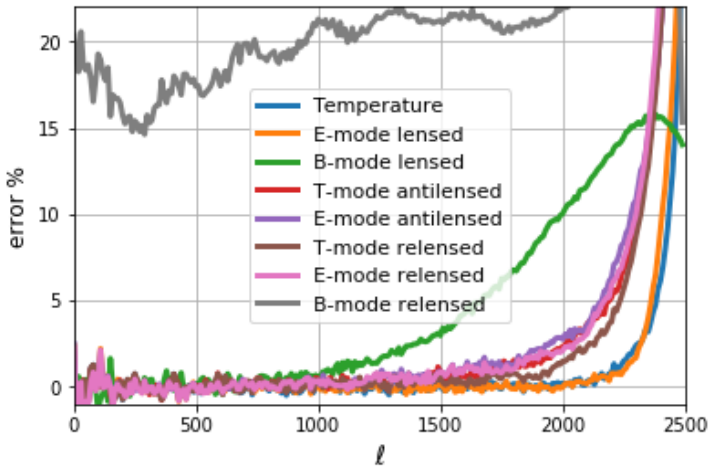

Figure 2.4: Percentage error $[1 - (C^{XX}_{\ell,\mathrm{LensPix}}/C^{XX}_{\ell,\mathrm{Model}})] \times 100$ between the respective lensed or unlensed `CAMB` model and `LensPix`'s lensed, antilensed, and relensed simulations. To compute these erros, `LensPix` C_ℓs were averaged over twenty five simulations of the same cosmological model.

Alternatively, the antilensing approximation simply takes the inverse displacement to be $d(\vec{n}) = -\nabla\phi(\vec{n})$, introducing, at leading order, errors of the order of $\nabla^b\phi \cdot (\nabla_a\nabla^a\phi)$. For a typical lensing

potential compatible with the standard cosmological model, this entails a maximum displacement of about $|\nabla^b\phi \cdot (\nabla_a \nabla^a \phi)| \sim 5.4'$. Going back to the characterization of the work simulations from the previous section, this is exactly where the error in the reproduction of lensed temperature and E-mode polarization maps starts to explote (see Figures 2.3 or 2.4 around $\ell \sim 180°/\theta \approx 2000$). This reflects the fact that `LensPix`'s lensing approximation is also of the first order [30].

To test whether the use of the antilensing approximation would limit our results, we lensed a set of CMB maps with a given $\nabla\phi$, then antilensed them with $-\nabla\phi$, and finally lensed them again. At each step, we computed the percentage error $[1 - (C^{XX}_{\ell,\mathrm{LensPix}}/C^{XX}_{\ell,\mathrm{Model}})] \times 100$ with respect to the corresponding lensed or unlensed model, showing the results in Figure 2.4. Note that the errors in the reproduction of the antilensed B-modes can not be calculated this way since our model does not consider primordial B-modes, which makes $C^{BB}_{\ell,unlens} = 0$. As can be seen in this figure, errors in the temperature and E-mode polarization maps do tend to accumulate with each lensing process. However, even after the second lensing, they remain of the order of or below the error committed in the simulation of the lensed B-mode polarization. Setting the same accuracy requirement than in the previous section, then the antilensing approximation would be enough for the delensing of temperature and E-mode polarization at the multipole range of interest $\ell < 1000$.

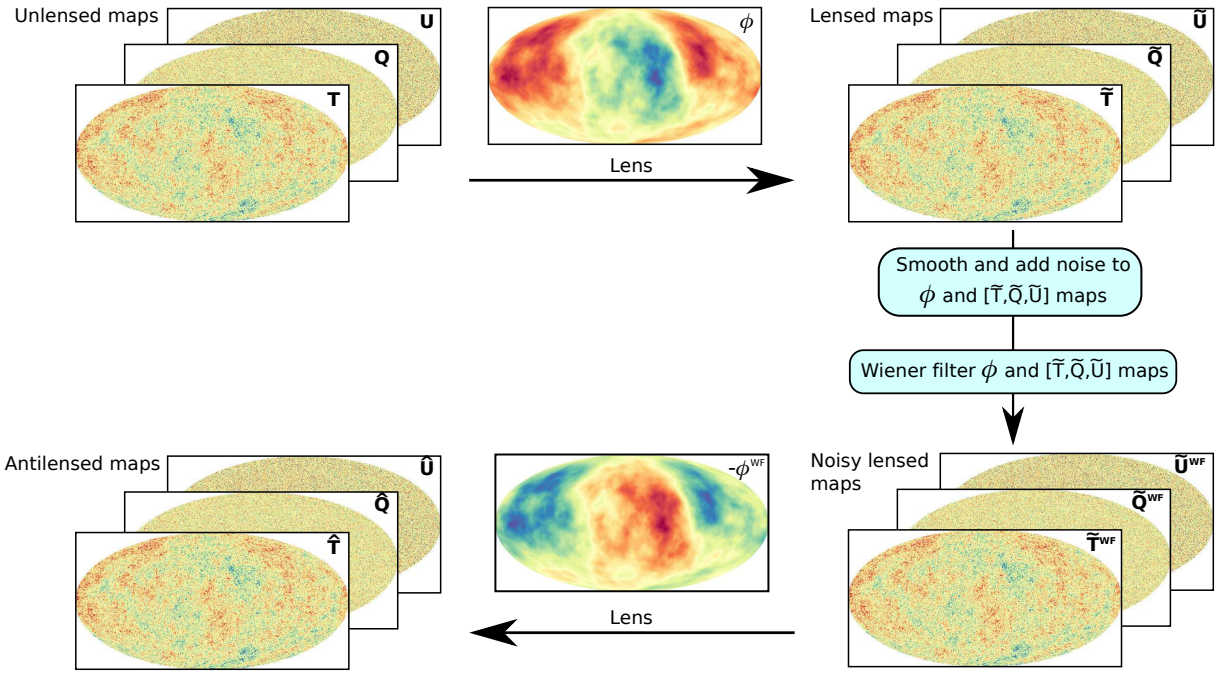

Figure 2.5: Flow diagram describing the pipeline of the delensing process. First, a random realization of CMB and lensing potential maps is computed. Then, after lensing the CMB with this potential, both the lensing potential and the output lensed CMB maps are degraded to a certain resolution and added a certain level of white noise. These degraded maps are then filtered to counteract the weight of the noise dominated scales. Finally, the antilensed CMB maps are obtained by lensing the Wiener filtered CMB maps with the opposite (also Wiener filtered) lensing potential.

In contrast, the error in the relensed B-modes is much higher. Again, this clearly shows the different nature of the lensing opperation for temperature and E-mode polarization, and B-modes. Since the antilensing approximation is accurate enough for temperature and E-mode polarization, and lensing and antilensing induced errors should accumulate at the same rate for B-modes than for temperature and E-modes, this different behavior is telling us that the explanation behind the inaccuracy in the reproduction of B-modes must be of a different kind. Therefore, we can assume that the antilensing approximation

is not the limiting factor in the reproduction of B-modes for $l < 1000$. Possible explanations for the inaccuracy in the simulation of B-mode polarization and solutions are further discussed in section 4.1.

With that said, we can now specify the pipeline of our delensing process. First, a random realization of CMB and lensing potential maps is computed. Then, after lensing the CMB with this potential, both the lensing potential and the output lensed CMB maps are degraded to a certain resolution each, and added a certain level of white noise to emulate the typical maps that may be expected from lensing reconstructions and future CMB experiments. As an additional step, these degraded maps are Wiener filtered to counteract the weight of noise dominated scales. This procedure is a common step in most delensing methods [33] [36] [27], and its relevance in our process will be discussed in section 2.4. Finally, the antilensed CMB maps are obtained by lensing the Wiener filtered CMB maps with the opposite (also Wiener filtered) lensing potential.

2.3 CMB maps and lensing potential reconstructions

As mentioned in the previous section, we *degraded* the quality of our simulated lensing potential and lensed CMB maps to resemble the ones that may be expected from future lensing reconstructions and CMB experiments. This degradation was implemented in two steps: first, we filtered the maps with a Gaussian window function to reduce their resolution, and then we added a certain level of white Gaussian noise.

The currently available best full-sky CMB maps, coming from ESA's *Planck* satellite, have noise levels of the order of tens of μK·arcmin for temperature and hundreds of μK·arcmin for polarization, with resolutions below $10'$ for its high-frequency bands [37]. From the next generation of space-based CMB experiments, like the already approved JAXA's LiteBIRD satellite, noise levels are expected to go down to about $2.5\mu K$·arcmin for polarization [38]. Particularly, LiteBIRD will have a typical resolution of $30'$, although some frequency bands will have a finer resolution of around $20'$. Complementary, experiments from the ground, like the CMB-S4, are expected to achieve even lower levels of noise ($\sim 1\mu K$·arcmin) and higher resolutions ($< 10'$) [39].

In this context, we chose to work with noises of $\sigma_n = 5, 3, 1\mu K$·arcmin, and to limit the resolution of our simulated maps to $\theta_{\mathrm{FWHM}} = 20', 10'$. As shown in the left panel of Figure 2.6, the effect this cut in resolution has, at the power spectrum level, is to suppress power at high multipoles. In turn, the power spectrum associated with each noise level can be calculated like

$$N_\ell = \frac{4\pi}{N_{pix}} \left(\frac{\sigma_n(\mu K \cdot arcmin)}{l_{pix}(arcmin)} \right)^2 , \tag{2.5}$$

where N_{pix} is the number of pixels in the map, and l_{pix} is the size of the pixel side. Note that although N_ℓ is a constant value, in Figure 2.6 it is represented as $\ell(\ell+1)N_\ell$, acquiring the observed $\sim \ell^2$ dependence. As can be seen in the left panel of Figure 2.6, the lensing signal is equivalent to a $5\mu K$·arcmin noise. In addition, these power spectra also evidence how, even when completely removing the lensing signal, sensitivities of around $1\mu K$·arcmin or lower would still be necessary to start detecting the primordial

B-mode spectrum at the largest scales.

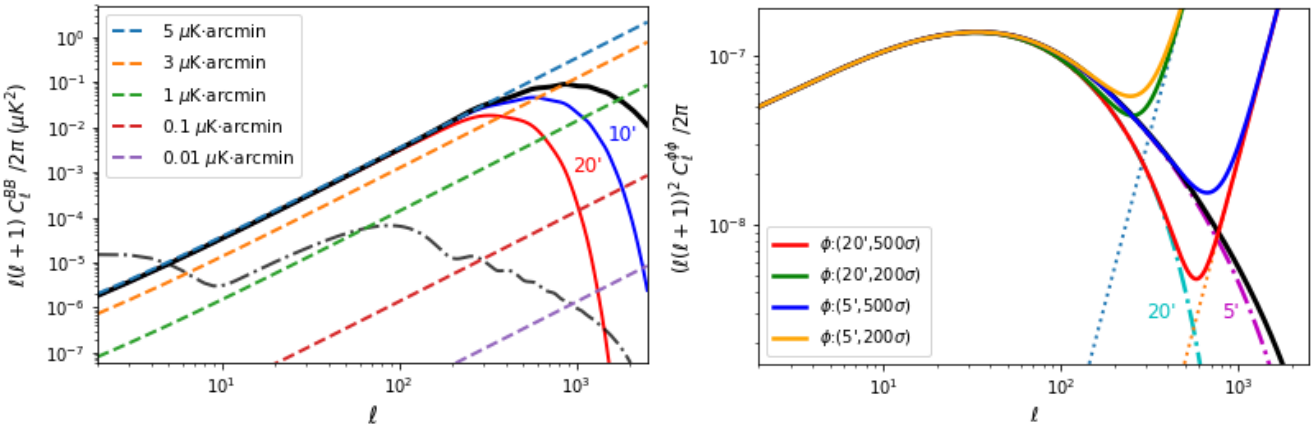

Figure 2.6: *Left panel:* Comparison between the lensing power spectrum at different resolutions and the power spectra associated to several levels of noise. The primordial B-mode spectrum for $r = 0.001$ (dashed black line) is also included as reference. *Right panel:* Lensing potential power spectrum after degrading it to a certain resolution and adding different levels of noise.

In contrast, for the lensing potential we chose the opposite approach: we artificially fixed certain resolutions and noise levels to evaluate the quality that future lensing potential reconstructions would need to achieve in order to amount to a given delensing fraction. Another difference with respect to the CMB map treatment is that we chose to identify the different levels of noise attending to the number of σ at which the lensing potential could be detected instead of using the actual value of the noise. The number of σ is computed from the angular power spectrum of the lensing potential and the noise angular power spectrum like:

$$\sigma_\phi = \left[\sum_{\ell=2}^{\ell_{max}} \left(\frac{C_\ell^{\phi\phi}}{C_\ell^{\phi\phi}+N_\ell}\right)^2 \left(\ell+\frac{1}{2}\right)\right]^{1/2}, \tag{2.6}$$

where $\ell_{max} = 2500$ for our simulations. This decision may seem peculiar, but it makes noise levels more manageable, since talking in terms of tens or hundreds of σs is far more intuitive than in terms of a $\sim [10^{-7}, 10^{-4}]$ adimensional noise. It also facilitates the comparison between our lensing potential reconstructions and the ones that can be found in the literature. As a reference, the *Planck* mission obtained a 40σ detection of the lensing potential with its full-mission results [27]. Compared to this recent result, the 200σ and 500σ levels we are going to assume may seem a bit far-fetched, and the discussion of its feasibility will be latter addressed in section 4.2. The effect this kind of noises have on the lensing potential power spectrum is shown in the right panel of Figure 2.6.

For the maps of the lensing potential, we fixed a default resolution of $5'$. This resolution was phenomenologically adopted after a quick test with different resolutions showed that it was the one that achieved the best delensing fractions, even slightly better than the ones coming from non-filtered noise-free lensing potential maps. This feature is probably just a numerical contraption since the main effect a $5'$ Gaussian window would have over a map with an initial $3.43'$ resolution would be to smooth out all the possible inhomogeneities produced in the numerical calculation of the lensing potential. We also explored resolutions of $20'$ and $10'$.

2.4 Wiener filtering

The Wiener filter is a powerful tool commonly applied in signal processing to disentangle signals from noisy data. It uses the knowledge of the statistical properties of both signal and noise to reconstruct an optimal estimation of the signal [40]. Although it was initially proposed in the domain of one-dimensional time-ordered signal processing, it can be generalized to the analysis of multidimensional data. In this framework, and assuming that the observed data vector d is a combination of the real signal s and some noise n, the Wiener filter is defined as

$$d^{WF} = \boldsymbol{S}(\boldsymbol{S} + \boldsymbol{N})^{-1} d, \tag{2.7}$$

where $\boldsymbol{S}$ and $\boldsymbol{N}$ are the covariance matrices of signal and noise, respectively. If both noise and signal follow a Gaussian distribution, then the Wiener filtered data d^{WF} is the maximum a posteriori solution for the estimation of the real signal. Since this is the case for the CMB, Wiener filtering is a common choice in most analysis processes, like power spectrum estimation, likelihood analysis, mapmaking and lensing reconstructions.

Figure 2.7 shows an example of how the Wiener filter works at the map level. Starting with a noise-dominated temperature map (left panel), the Wiener filter is able to produce a map that is signal-dominated at large and intermediate angular scales (central panel), at the cost of losing part of the information at the smallest scales. This means that, when comparing the Wiener filtered map with the true signal (right panel), the finer details present in the true signal seem to have been smoothed out in the filtered map.

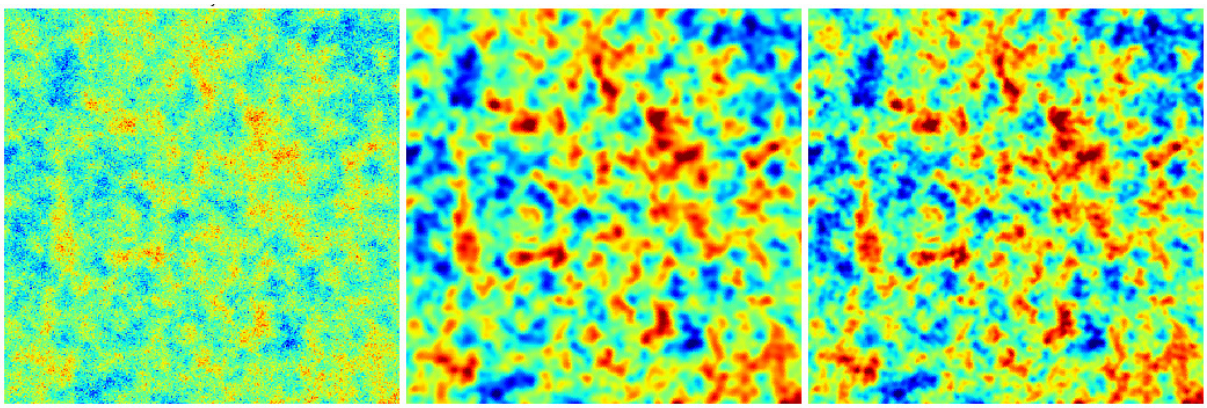

Figure 2.7: Example of how the Wiener filter works at the map level. Starting with a noise-dominated temperature map (left panel), the Wiener filter is able to produce a map that is signal-dominated at all scales (central panel), at the cost of losing part of the information at the smallest scales. In such manner, the Wiener filtered map looks like a smoothed version of the true signal (right panel).

At the power spectrum level, the Wiener filter definition from equation (2.7) can be written in terms of the signal (C_ℓ^s) and noise angular power spectra like [41]

$$d_{\ell m}^{WF} = \frac{C_\ell^s}{C_\ell^s + N_\ell} d_{\ell m}, \tag{2.8}$$

where $d_{\ell m}$ corresponds to the power spectrum of the observed noisy data. Expressed this way, it becomes obvious to see how the Wiener filter will suppress power at noise-dominated scales. For the CMB temperature spectrum, noise starts to dominate over signal at small scales (high ℓ), which is why

the Wiener filtered map from the previous example lacked the finer structure encoded in the smallest scales.

In particular, our implementation of the Wiener filter takes the form of

$$X_{\ell m}^{WF} = \mathcal{W}_\ell^{WF} X_{\ell m}^{obs}; \qquad \mathcal{W}_\ell^{WF} = \frac{1}{\omega_\ell} \frac{X_\ell^{model}}{X_\ell^{model} + N_\ell \omega_\ell^{-2}}. \tag{2.9}$$

With this formulation, we also take into account the effects of the Gaussian window ω_ℓ used to limit the map resolution. The expression for thise Gaussian window, as a function of multipole ℓ, is

$$\omega_\ell = e^{-\ell(\ell+1)\theta^2_{\mathrm{FWHM}}/8\ln 2}. \tag{2.10}$$

We applied this filter to all of our maps, both the CMB and lensing potential ones, so the X term in equations (2.9) runs for $X = C^{TT}, C^{EE}, C^{BB}, C^{\phi\phi}$. The effect the filter has over the B-mode polarization power spectrum of CMB maps when several levels of the noisy are added can be seen in Figure 2.8. The actual value that the filter window $\mathcal{W}_\ell^{WF}$ takes for each scale is shown in the right panel, demonstrating how the dominance of noise at the smallest scales (high ℓ) leads to the suppression of power. Another important observation is the fact that for high enough levels of noise, power will also start to be suppressed at large scales (small ℓ). Amongst the considered noise levels, this is especially relevant for the $5\mu K\cdot$arcmin case, where the noise and signal are of the same order for multipoles $\ell < 300$ (see the left panel of Figure 2.6), causing the Wiener filtered power spectrum to be about a half of the original one.

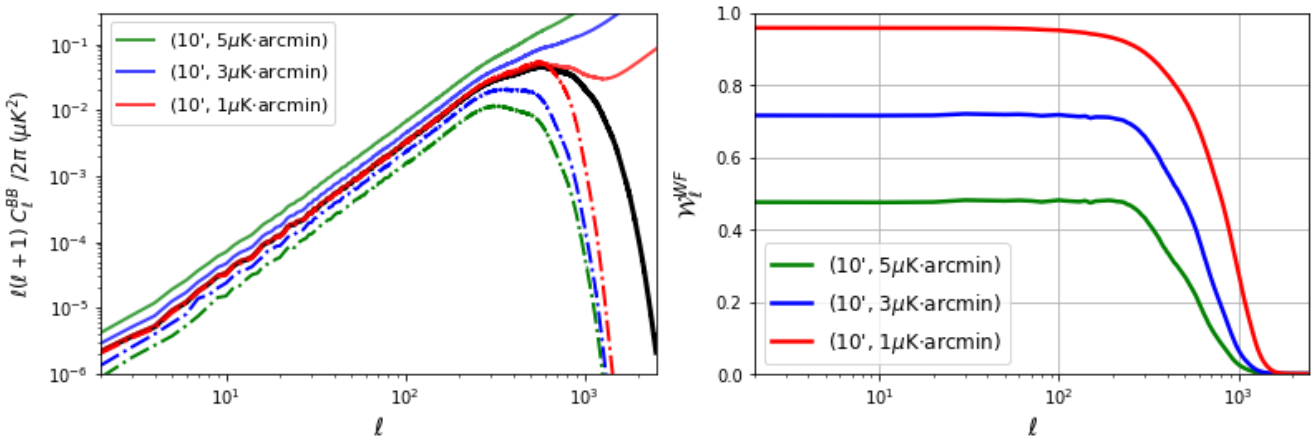

Figure 2.8: *Left panel:* B-mode power spectrum of noisy CMB maps before (solid curves) and after (dash-dotted curves) Wiener filtering. The model spectrum is included as a solid black line for reference. *Right panel:* Value the Wiener filter window $\mathcal{W}_\ell^{WF}$ takes at every multipole for each of the noise levels shown in the left panel.

As it was already mentioned, Wiener filtering is a common practice in most of the data analysis involving CMB maps, and in our case it turned out to be a key step in the delensing process. Delensing completely relies on the fact that the lensed map is just a remapped version of the unlensed one, but with the introduction of noise, which randomly distorts the lensed map, this equivalence starts to fail. For high enough noise amplitudes, the noisy lensed map is so different from the initial one that lensing it with $-\nabla\phi$ effectively acts as a new lensing rather than a delensing. As a consequence, the B-mode power spectrum of a noisy "delensed" map can be greater than the initial lensed spectrum.

This is what happened to our first set of antilensed maps when noises above $1\mu K\cdot$arcmin were added. The solution to this problem was the use of the Wiener filter to keep noisy maps as close to the true signal

as possible. The results presented in the following chapter demonstrate how this approach works fine for noises below $5\mu K$·arcmin. As one can imagine from the previous discussion, $5\mu K$·arcmin is the limit at which not even the Wiener filter can keep the noisy lensed map similar enough to the true lensed map to allow a successful delensing. Therefore, a $5\mu K$·arcmin noise is the natural limit at which delensing processes of all kinds start to fail [42].

CHAPTER 3

Results

3.1 Delensing fractions

In this section we will present the main results of our study, leaving the discussion of the implications they have on the detectability of the tensor-to-scalar ratio for the next section. The most immediate result, the B-mode angular power spectrum of the delensed maps, is shown in Figure 3.1. For clarity, only some of the combinations of degraded CMB and lensing potentials specified in section 2.3 were included. This graph shows how, except for the case were a noise of $5\mu K\cdot$arcmin was added, our antilensing process does indeed reduce the B-mode power spectrum. More specifically, at large scales, the antilensed spectrum seems to be just a fraction of the lensed one. Therefore, we could model delensing as a reduction in the lensed power spectrum of $C^{BB}_{\ell,antilensed} = \mathcal{D}\, C^{BB}_{\ell,lensed}$, where $\mathcal{D}$ is a constant number, (ideally) smaller than one. We will refer to this $\mathcal{D}$ as the *delensing fraction*.

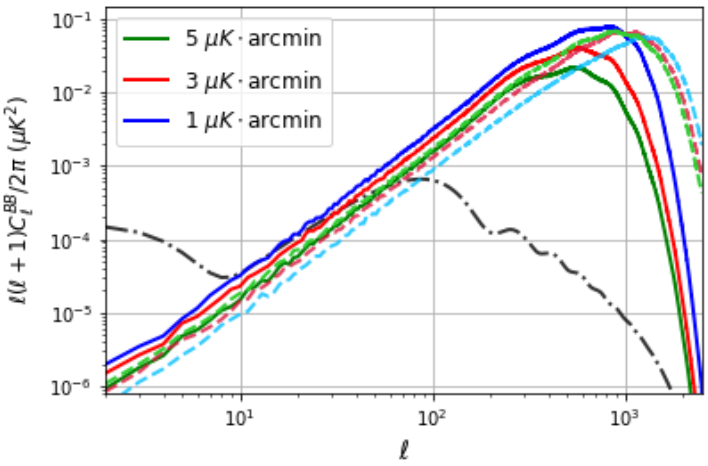

Figure 3.1: Comparison between the B-mode power spectrum of the starting Wiener filtered map (solid curves) and the output antilensed map (dashed curves of a fairer color). All three delensings were performed with a lensing potential of $\phi : (5', 500\sigma)$, and starting with a CMB map of $\theta_{\mathrm{FWHM}} = 10'$ resolution. The primordial B-mode power spectrum corresponding to $r = 0.001$ (dash-dotted black line) is included as reference.

The other remarkable feature evidenced by this plot is the fact that the antilensed spectra show more power at small scales than the lensed ones. This extra power may seem surprising at first, but it is a natural product of the delensing process since the small scales suppressed by the Wiener filter in our lensed maps differ enough from the true signal to receive delensing as a new lensing, thus recovering part of the original lensed spectrum. Once the origin of this power excess is understood, the only consequence it

has on the analysis is the limitation of the multipole range at which our simple model of delensing with a constant $\mathcal{D}$ is valid. Such proportionality relation between lensed and antilensed spectra is examined in greater detail in Figure 3.2, where the delensing fraction is plotted as a function of multipole. In this graph, we can clearly see how delensing fractions are indeed approximately constant for $\ell \lesssim 100$. This multipole range is roughly sufficient from the point of view of detecting primordial B-modes since the signal starts to intrinsically diminish at scales smaller than that. Also we can easily identify the multipole at which the antilensed spectra start to overpower the lensed ones as the ℓ at which $\mathcal{D}_\ell$ explotes towards values greater than one.

Since more combinations of degraded CMB and lensing potentials were included this time, we can also start to discuss the phenomenology of the different cases. But before jumping to that, let us explain the two special cases that standout in Figure 3.2: the yellow curves with delensing fractions greater than one, and the black curve at the bottom. The yellow curves are those associated to CMB maps where $5\mu K$·arcmin noises were added, and based on previous discussion, it should not be a surprise that they present delensing fractions greater than one. A noise level of $5\mu K$·arcmin has the same power as the lensing signal, and consequently, the Wiener filtered version of such noisy map would be so different from the original lensed signal that it would receive delensing as a new lensing.

The black curve, however, illustrates a more alarming feature. It corresponds to the delensing fraction obtained when the exact lensed map is antilensed with the original lensing potential, without the addition of any noise or beam to either map. Theoretically, in such ideal scenario lensing should be completely reversed, and the fact that a residual lensing signal remains is just another manifestation of the difficulties the `LensPix` code has with the simulation of B-mode polarization. Therefore, it exists a maximum delensing fraction this tool can achieve. For our cosmological model, this limit is of $\mathcal{D} = 0.09$. For now, we will just acknowledge the existence of this feature and treat it as the floor that marks the maximum delensing fraction possible, assuming that it does not hinder the delensing fractions obtained in all the other studied cases since the degradation of CMB and lensing potential maps should play a more dominant role. Nevertheless, the validity of this assumption will be further examined in section 4.1.

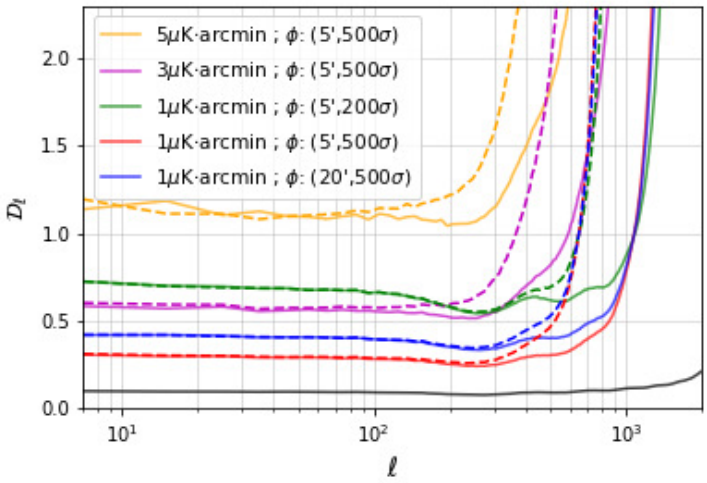

Figure 3.2: Delensing fractions, as a function of multipole, obtained for some of the different CMB and lensing potential combinations explored. Solid curves correspond to CMB maps of $\theta_{\mathrm{FWHM}} = 10'$ resolution, while dashed curves are those of $\theta_{\mathrm{FWHM}} = 20'$ resolution CMB maps. The solid black line shows the maximum delensing fraction that can be achieved with `LensPix` for our cosmological model.

A first qualitative analysis of the curves in Figure 3.2 tells us how the main factor in the determination of the delensing fraction is the quality of the lensing potential reconstruction, especially the number of σ at which it is detected (green curves compared to the red ones). In comparison, the limitation imposed by the resolution of the lensing potential map is of lesser importance (leap between red and blue curves). In terms of the quality of CMB maps, a reduction of the noise level plays a similar role in the improvement of the delensing fraction than an increase in the quality of the lensing potential reconstruction (difference between magenta and red curves). On the other hand, the resolution of CMB maps seems to have a dual behavior (dashed curves overlaid with the solid ones): at small scales, it fixes the maximum multipole up to which $\mathcal{D}_\ell$ remains approximately constant and lower than one; while at large scales, delensing fractions are not sensitive to an improvement in the resolution of the CMB map.

Such behavior is just a reflection of the role the Gaussian beam ω_ℓ plays in the construction of the Wiener filter window (remember equations (2.10) and (2.9) from section 2.4). At large scales, its effect is neglegible, allowing the value of the window function to be completely determined by the ratio of signal and noise. In contrast, its contribution becomes significant at large multipoles, boosting the step fall in the window function and, therefore, helping to produce the suppression of power at small scales observed in Wiener filtered maps. In turn, as previously discussed, it is the contrast between the lack of power at small scales of Wiener filtered maps and the way it gets created again in the delensing process what produces the growth of delensing fractions to values much greater than one at high multipoles.

A deeper analysis of the phenomenology would require a quantitative measure of the delensing fraction associated to every CMB and lensing potential combination. To obtain those values, we averaged the quotient between antilensed and lensed power spectra over the first hundred ℓ:

$$\mathcal{D} = \left\langle C^{BB}_{\ell,antilensed} / C^{BB}_{\ell,lensed} \right\rangle_{\ell \leq 100} . \tag{3.1}$$

Looking at the multipole dependence $\mathcal{D}_\ell$ presents in Figure 3.2, $\ell \leq 100$ is the multipole range where delensing fractions remain approximately constant. Applying this criterion, we calculated the delensing fractions shown in Table 3.1 and plotted in Figure 3.3 as a function of the number of σs of the lensing potential reconstruction (left panel) and the noise level of CMB maps (right panel). For completeness, we explored here more combinations of CMB maps and lensing potential qualities than those discussed in section 2.3.

σ_n [μK·arcmin] \ ϕ	$(5', 50\sigma)$	$(5', 200\sigma)$	$(20', 500\sigma)$	$(10', 500\sigma)$	$(5', 500\sigma)$	$(5', 700\sigma)$
5	1.00	1.03	1.08	1.10	1.11	1.13
3	0.96	0.79	0.63	0.58	0.56	0.52
1	0.95	0.68	0.41	0.32	0.29	0.21
0.1	0.94	0.67	0.38	0.29	0.26	0.17

Table 3.1: Delensing fraction, calculated following equation (3.1), for each combination of degraded CMB map and lensing potential reconstruction explored. The given values correspond to a CMB map resolution of $\theta_{\mathrm{FWHM}} = 10'$. However, as can be seen in Figures 3.2 and 3.3, delensing fractions are almost identical for $10'$ and $20'$ resolutions for $\ell \lesssim 100$.

Drawn this way, it is easy to understand the effect both properties of the input maps have on the determination of the delensing fraction. As a function of the noise level of CMB maps, delensing frac-

tions can be perfectly fitted by a phenomenological $a\sigma_n^2 + b$ curve, with the quality of lensing potential reconstructions fixing how flat or step the curve is. Thus, once the quality of the lensing potential is set (*i.e.*, the values of a and b are determined), the maximum delensing fraction that can possibly be achieved by improving the noise level of the input CMB map is also fixed. Remembering the difficulties delensing faces near the $5\mu K$·arcmin limit, we could use this simple law to predict the noise level at which delensing would start to be profitable, *i.e.*, the σ_n at which $\mathcal{D}$ becomes smaller than one. Without stopping in individual cases, a delensing fraction smaller than one is possible for all studied combinations as long as the CMB map noise is below $\sigma_n = 4.5\mu K$·arcmin.

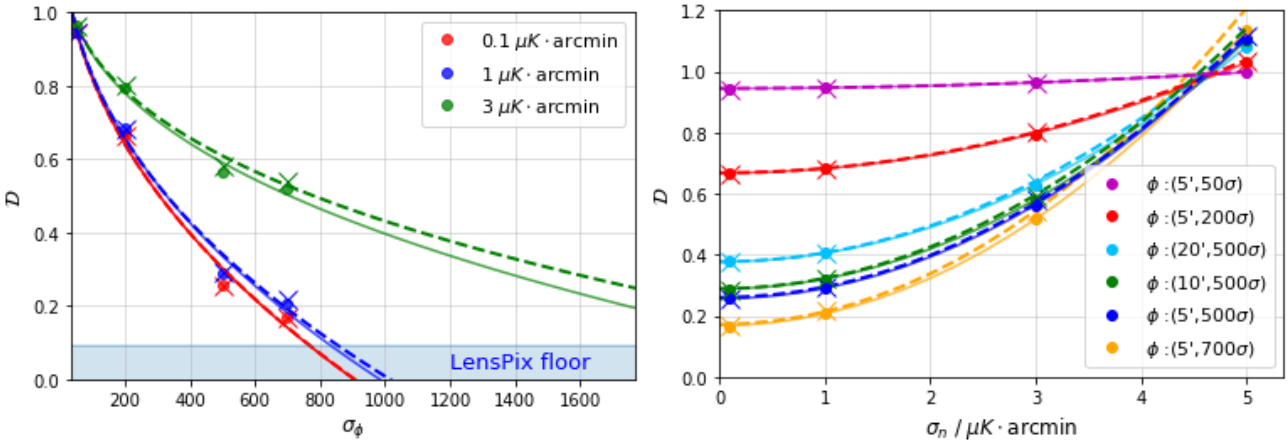

Figure 3.3: Behavior of delensing fractions as a function of the quality of the lensing potential reconstruction (left panel) and the noise level of CMB maps (right panel). In both graphs circles and solid lines correspond to a CMB map resolution of $\theta_{\rm FWHM} = 10'$, while crosses and dashed lines are associated with a $\theta_{\rm FWHM} = 20'$ resolution. When plotting the delensing fraction as a function of the number of σs of the lensing potential reconstruction, only the values associated to a $5'$ filtered ϕ were included.

On the other hand, the dependence delensing fractions have with the number of σs of the lensing potential reconstruction can be approximated by a simple power law like $a\sigma_\phi^n + b$, with exponents of $n \sim 0.43$ for CMB noises of $\sigma_n = 0.1, 1\mu K$·arcmin, and $n \sim 0.36$ for $\sigma_n = 3\mu K$·arcmin. Therefore, in this other scenario where the noise and resolution of the input CMB map are fixed, delensing fractions could, in principle, continuously be reduced down to $\mathcal{D} = 0$ by improving the quality of the lensing potential reconstruction.

However, there is a restriction on the maximum value both σ_ϕ and $\mathcal{D}$ can have. The limit for the delensing fraction is the already introduced $\mathcal{D} = 0.09$ `LensPix` floor. Based on the power laws we fitted, lensing potential reconstructions would need to achieve a quality of about 770σ, 836σ and 2275σ in order to reach the `LensPix` floor when applied to CMB maps with noise levels of $0.1\mu K$·arcmin, $1\mu K$·arcmin and $3\mu K$·arcmin respectively. In addition, the number of σs of the lensing potential reconstruction can not indefinitely increase since it is limited by the number of available multipoles. Going back to its definition in equation (2.6), this means that when no noise is added, the sumatory of the term $(\ell + \frac{1}{2})$ determines the maximum σ_ϕ possible. Summing up to $\ell_{max} = 2500$, this limit is of $\sigma_\phi^{max} = 1769$. Therefore the `LensPix` floor would not be reachable for a CMB input map with a $3\mu K$·arcmin noise. Instead, for this case the maximum delensing fraction produced at σ_ϕ^{max} would be $\mathcal{D} = 0.19$.

3.2 Detectability of the tensor-to-scalar ratio

Having studied what kind of delensing fractions can be achieved, let's see now the impact they have on the detection of a primordial B-mode. For our discussion in detectability to be more realistic, in addition to lensing and instrumental noise we can also take into account the contribution of galactic foregrounds. Starting from the foreground spectrum expected for the 1% cleanest fraction of the sky at 100GHz, we will assume that component separation techniques were able to further reduce that foreground signal down to its 1%, which is in agreement with the ongoing forecasting in the literature (*e.g.*, [43]), and add it as part of the observed B-mode polarization. As an example, Figure 3.4 shows what would be the observed B-mode polarization spectrum after having performed delensing with a 500σ lensing potential reconstruction over a CMB map of $10'$ resolution and $1\mu K{\cdot}$arcmin noise ($\mathcal{D} = 0.29$) when including the described residual foreground component and the primordial B-mode generated by a PGW spectrum of $r = 1 \times 10^{-3}$. As one can see, even in this favorable scenario, the detection of such a faint primordial B-mode is not easy.

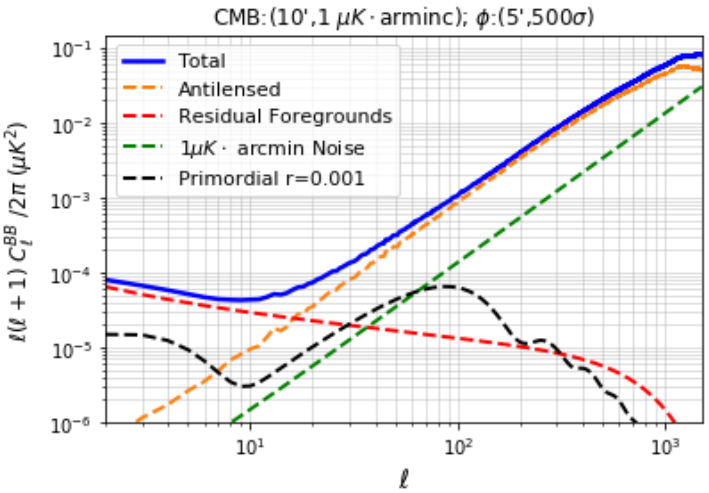

Figure 3.4: B-mode power spestrum after performing delensing with a 500σ lensing potential reconstruction over a CMB map of $10'$ resolution and $1\mu K{\cdot}$arcmin noise, and assuming that component separation techniques have reduced to its 1% the expected foreground spectrum at 100GHz from the 1% cleanest fraction of the sky. The foreground angular power spectrum was obtained as an approximated law estimated from [43]. A primordial B-mode generated by a PGW spectrum of $r = 1 \times 10^{-3}$ is considered.

We will evaluate the degree of detectability of the primordial B-mode spectrum as a function of its amplitude, quantified by the tensor-to-scalar ratio r, through the signal-to-noise ratio:

$$S/N(r) = \left[\sum_{\ell=2}^{1000} \left(\frac{rB_\ell^{prim}}{rB_\ell^{prim} + L_\ell + N_\ell \omega_\ell^{-2} + F_\ell}\right)^2 \left(\ell + \frac{1}{2}\right)\right]^{1/2}, \tag{3.2}$$

where B_ℓ^{prim} is the primordial B-mode spectrum for an $r = 1$, L_ℓ is the antilensed B-mode spectrum, and F_ℓ the residual foreground spectrum. Summing only up to $\ell = 1000$, the limit set in section 2.1 to guarantee a good accuracy in the simulation of B-mode polarization, we are dismissing the signal carried by higher multipoles. However, since the primordial B-mode contribution is only relevant at the largest scales ($\ell < 100$), the signal-to-noise ratio should not be significantly affected by this restriction of available multipoles. The left panel of Figure 3.5 shows the signal-to-noise ratios obtained this way for the delensing scenarios previously contemplated in Figure 3.2. As can be seen, signal-to-noise quickly falls towards smaller tensor-to-scalar ratios, with only the cases with a $1\mu K{\cdot}$arcmin noise and delensing

fractions $\mathcal{D} < 0.55$ (blue and red curves) reaching a signal-to-noise ratio above the high-confidence detection threshold of $S/N = 5$ at $r = 1 \times 10^{-3}$. For $r < 6 \times 10^{-4}$, a solid $S/N = 5$ detection stops being possible in all considered scenarios.

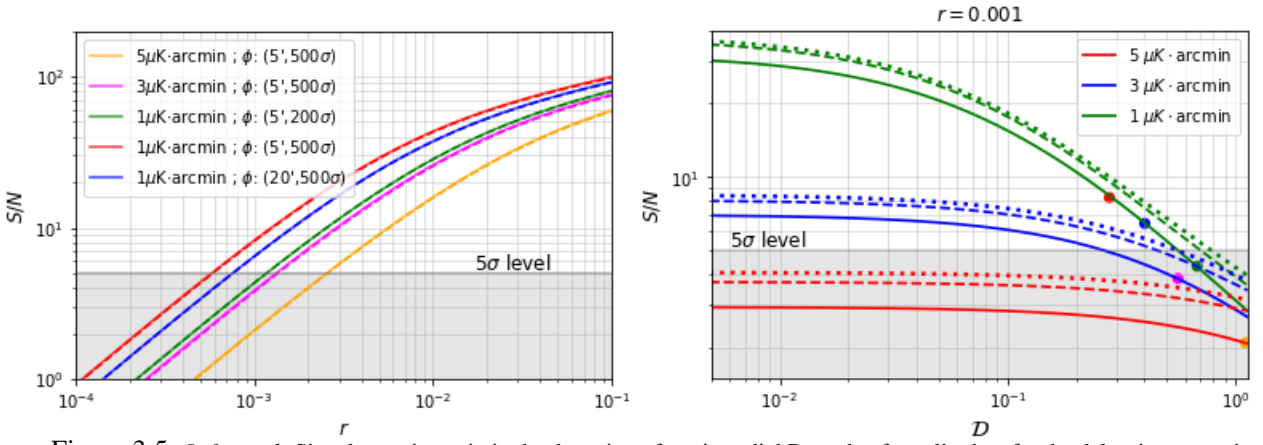

Figure 3.5: *Left panel:* Signal-to-noise ratio in the detection of a primordial B-mode of amplitude r for the delensing scenarios considered in Figure 3.2. Solid lines correspond to a CMB map resolution of $\theta_{\rm FWHM} = 10'$, and dashed ones to $\theta_{\rm FWHM} = 20'$. The shaded area highlights the signal-to-noise ratios below the common $S/N = 5$ detection threshold. *Right panel:* Increase in signal-to-noise gained by improving the delensing fraction for a primordial B-mode spectrum of $r = 1 \times 10^{-3}$. For the solid curves we assumed component separation techniques achieved a 1% reduction of the expected foreground signal, while 0.1% and 0.01% reductions were assumed for the dashed and dotted curves respectively. The colored points locate where the delensing scenarios from the previous $S/N(r)$ graph fall in this new representation of $S/N(\mathcal{D})$.

Signal-to-noise could obviously be improved by increasing the delensing efficiency, either by reducing the noise of the CMB map or enhancing the quality of the lensing potential reconstruction. However, a reduction of the delensing fraction will not always be helpful, because at some point the noise and foreground contributions will start to dominate the signal-to-noise. Since at large scales the lensed B-mode spectrum behaves practically like white noise, noise will start to dominate once the delensing fraction is low enough to bring lensed B-modes below its spectrum, and any improvement in the delensing efficiency will prove irrelevant (see how signal-to-noise saturates for low values of $\mathcal{D}$ in the right panel of Figure 3.5). A reduction of the foreground signal frees the largest scales, and although it will result in an overall increase in the signal-to-noise until the valley in the primordial B-mode spectrum at $\ell \sim 10$ is uncovered (dashed and dotted lines compared to the solid ones), the relation between noise and lensed B-modes stills dictates the behavior of $S/N(\mathcal{D})$.

Until now we have been discussing what delensing efficiencies could be possible if delensing with a certain lensing potential reconstruction was applied to a given CMB experiment, but through an study of this kind that allows us to understand the contribution each different component has in the overall signal-to-noise, one could propose the opposite question: what would be the optimal delensing fraction for a given CMB experiment, and what kind of lensing potential reconstruction would be needed to meet it? As an example, Table 3.2 shows the delensing fractions for which a $S/N = 5$ detection of a primordial B-mode of amplitude $r = 1 \times 10^{-3}$ would be possible for two different scenarios of CMB noise and foreground residual signal. Next to them, we include the quality requirements that the lensing potential reconstruction would need to meet to achieve those delensing fractions based on the power laws we fitted in the previous section. Like the discussion on lensing potential reconstruction feasibility of section 4.2 will show, while the ones required for the $1\mu K{\cdot}$arcmin may be viable for future experiments, internal lensing potential reconstruction will not achieve the required quality to reach a $S/N = 5$ detection for CMB maps with a $3\mu K{\cdot}$arcmin.

	1% foregrounds		0.1% foregrounds	
σ_n /μK·arcmin	$\mathcal{D}_{S/N=5}$	σ_ϕ	$\mathcal{D}_{S/N=5}$	σ_ϕ
3	0.27	1449	0.46	813
1	0.56	275	0.71	165

Table 3.2: Prediction of the delensing fractions, and quality of the lensing potential reconstruction necessary to reach them, that would be requiered to achieve a $S/N = 5$ detection of a primordial B-mode of amplitude $r = 1 \times 10^{-3}$ in two different scenarios of CMB noise and foreground residual signal.

However, although this may seem a little discouraging, delensing should still be part of any attempt at primordial B-mode detection. To illustrate the validity of this point, Figure 3.6 shows the fractional gain

$$G = \frac{S/N_{\text{w/ delensing}}}{S/N_{\text{w/o delensing}}} \tag{3.3}$$

in signal-to-noise attained for performing delensing for the scenarios considered in the left panel of Figure 3.5. As this figure shows, the lower the tensor-to-scalar ratio is, the more primordial B-mode detection benefits from delensing. Again, the gain starts to saturate once the amplitude of the primordial spectrum is so low that it is completely obscured by the other contributions.

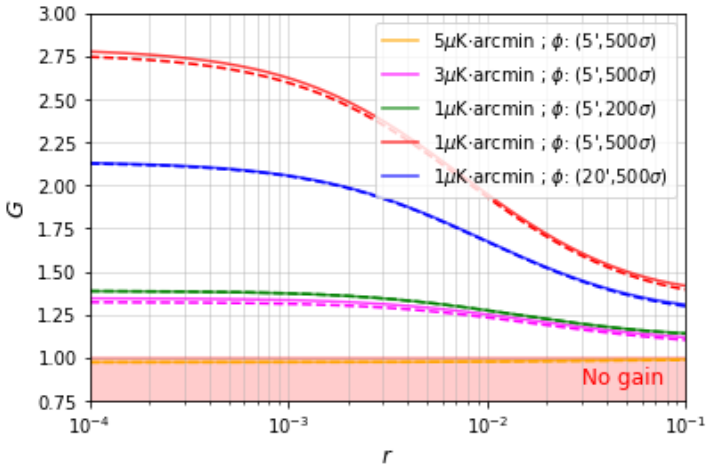

Figure 3.6: Fractional increase in signal-to-noise gained for performing delensing as a function of the tensor-to-scalar ratio. Displayed in red is the region where delensing does not report any profit to the increase in signal-to-noise. Solid lines correspond to a CMB map resolution of $\theta_{\text{FWHM}} = 10'$, and dashed ones to $\theta_{\text{FWHM}} = 20'$.

Another approach to evaluate detectability would be to determine what confident interval around the best fit value of the tensor-to-scalar ratio one would obtain if they were to fit a primordial B-mode spectrum as part of the observed B-mode polarization. In this way, we could assume a certain primordial B-mode plus noise and foreground residuals and a given delensed B-mode spectrum as the model to fit, and use the χ^2 statistic to measure the goodness of fit:

$$\chi^2(r, A_L) = \sum_{\ell=2}^{1000} \frac{\left(B_{obs} - rB_\ell^{prim} - A_L L_\ell - A_F F_\ell - N_\ell \omega_\ell^{-2}\right)^2}{\sigma_\ell^2}, \tag{3.4}$$

where the error at each multipole would be the cosmic variance associated to the fiducial observed B-mode polarization

$$\sigma_\ell^2 = \frac{B_{obs}^2}{(\ell + 0.5)} = \frac{\left(r_{fid} B_\ell^{prim} + L_\ell + N_\ell \omega_\ell^{-2} + F_\ell\right)^2}{\ell + 0.5}. \tag{3.5}$$

In equation (3.5), like in the rest of this work, we are assuming an ideal case of full-sky coverage. Otherwise, a f_{sky}^{-1} should be added to the cosmic variance to account for the so-called *sampling variance*. The Fisher matrix, defined from the χ^2 like

$$\mathcal{F}_{ij} = \frac{1}{2}\frac{\partial^2\chi^2}{\partial\theta_i\partial\theta_j}, \tag{3.6}$$

can then be used to approximate the covariance matrix $C = \mathcal{F}^{-1}$ [44], which contains in its diagonal elements the uncertainties of the parameter estimation $C_{ii} = \sigma^2_{\theta_i}$, and the correlated uncertainties in the rest $C_{ij} = \sigma_{\theta_i\theta_j}$. Once the covariance matrix is known, the likelihood function around the fiducial value of the model's parameters is just

$$\mathcal{L}(\theta) = \frac{1}{(2\pi)^{N/2}|C|^{1/2}} e^{-\frac{1}{2}(\theta-\theta_{fid})C^{-1}(\theta-\theta_{fid})^\dagger}, \tag{3.7}$$

and confidence contours can be drawn as indicated in [45]. If the parameters are Gaussian-like distributed, the confidence contours obtained through the Fisher matrix are exact, and even if they are not, the Fisher matrix still provides a reasonable approximation around the point of maximum likelihood. We checked the Fisher contours against a MCMC sampling of the full likelihood function, and found them to be more than enough for this relatively simple case.

Following this formalism, 1σ (68%) and 2σ (95%) contours are drawn in Figure 3.7 for a fiducial $r = 6 \times 10^{-4}$ and different delensing scenarios. In this case, detection is possible when the confidence interval is lower than the considered tensor-to-scalar ratio (*i.e.*, contours do not cross zero). Note that now the detection of a given tensor-to-scalar ratio will be harder than discussed in previous pages since we are fitting three parameters (r, A_L and A_F) instead of one, and the uncertainties of these marginalized parameters will grow. Even so, with delensing fractions of $\mathcal{D} = 0.56$ and $\mathcal{D} = 0.68$ respectively for CMB maps with noises of $3\mu K$·arcmin and $1\mu K$·arcmin (green and blue contours) we would be close to a 2σ detection of a primordial B-mode of $r = 6 \times 10^{-4}$ amplitude, which is a high enough confidence interval to be commonly accepted in forecasting. Although such contours are not included here, the $1\mu K$·arcmin case with a $\mathcal{D} = 0.29$ (red contour) would be detected by more than 3σ.

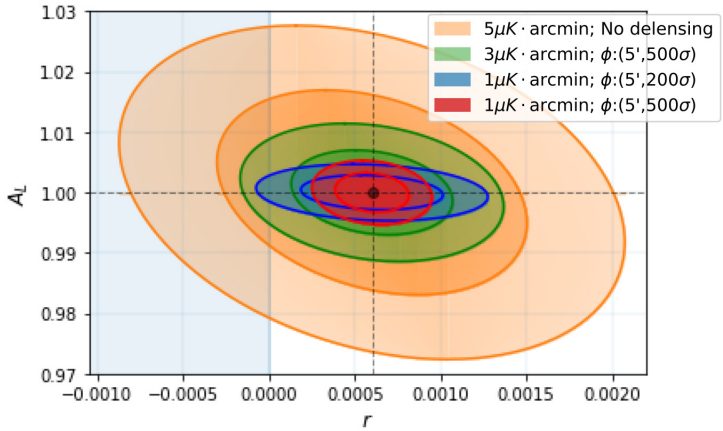

Figure 3.7: 1σ and 2σ confidence contours in the estimation of the r and A_L parameters after marginalizing over A_F, when a fiducial $r = 6 \times 10^{-4}$ and different delensing scenarios are assumed. Since delensing does not reduce lensed B-mode for CMB maps with a $5\mu K$·arcmin noise, confidence contours for that case are calculated just using the Wiener filtered lensed B-mode spectrum.

When greater values of r are assumed, detections start to be extensively met for the all the scenarios shown in Figure 3.7, getting to the point where a 2σ detection of a primordial B-mode with $r > 15 \times 10^{-4}$ would be possible even without delensing and a noise level of $5\mu K$·arcmin. This is why experiments like LiteBIRD plan to rely on just a good reduction of galactic foregrounds and a low level of noise to allow the detection of primordial B-modes without bothering on delensing.

CHAPTER 4

Discussion

4.1 LensPix limitations and implications for our results

Throughout this work, we have seen time and again how `LensPix` does not have the same accuracy in the reproduction of lensed B-modes than for the lensing of temperature and E-mode polarization. This reflects the intrinsically different nature of lensing for these fields: for temperature and E-mode polarization, lensing is a self-contained operation with no need of external information; meanwhile, lensed B-modes are entirely created by the leakage of E-modes. In addition, lensed B-modes constitute a very faint signal (between two to five orders of magnitude lower than E-modes and temperature for an $r = 0.001$), that when no primordial B-mode is considered, has to be completely transferred from E-mode polarization. Given the observed performance, there is clearly some operation during this transference process that is introducing a large numerical error.

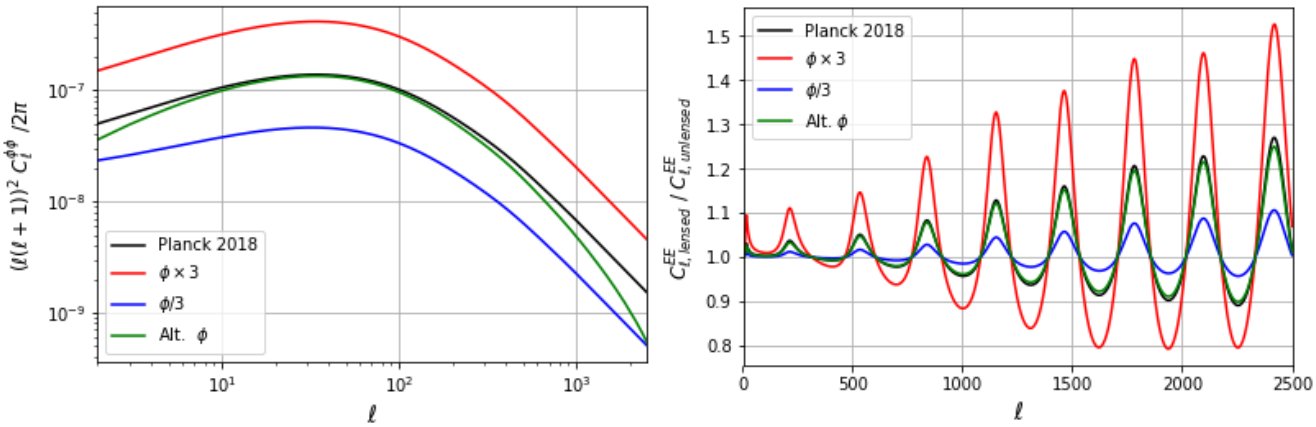

Figure 4.1: *Left panel:* Lensing potentials used to explore how the importance of the lensing contribution affects the accuracy of the lensing process. Lensing potentials in blue and red are simply multiples of the *Planck* 2018 potential, while the green one corresponds to an alternative cosmology where a greater σ_8 was assumed. *Right panel:* Effect lensing has on E-mode polarization when it is performed with the lensing potentials shown in the left panel.

Following this line of thought, we ran a few tests to try to identify where the inaccuracy is coming from. We simulated the lensing of several artificial CMBs with especially low and high C_ℓ^{EE} power spectra to test if errors increased or decreased when working with fainter or higher signals, and ran a couple of simulations including primordial B-modes to see if lensed B-modes were better computed when an initial signal alreadey existed. We found that no significant error seemed to be introduced or lessened in the reproduction of the lensing of either E- and B-modes in any of these cases.

However, the accuracy in the reproduction of lensed fields does depend on the importance of the lensing contribution. To check that, we lensed the same initial CMB model with the different lensing potentials displayed in the left panel of Figure 4.1. As can be seen in the right panel of that Figure, a change in the amplitude of the potential will produce a greater or smaller lensing contribution (red and blue lines), while the subtle loss of power at the largest and smallest scales of the alternative lensing potential (green line) does not significantly affect lensing. Contrary to what could be expected, `LensPix` reproduces better the lensing of E-mode polarization when the lensing contribution is smaller, and is not sensitive to the change of lensing potential (see Figure 4.2). The opposite happens for the lensing of B-mode polarization: a better accuracy is obtained when lensing has a greater contribution, and errors strongly depend on the shape of the lensing potential spectrum.

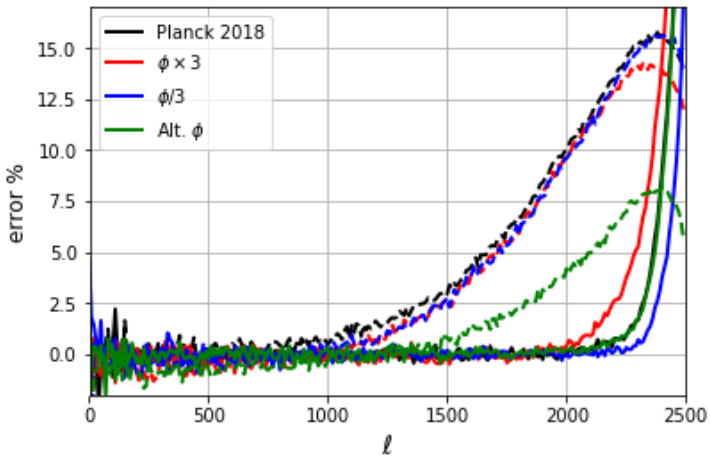

Figure 4.2: `LensPix` accuracy to reproduce the lensing of the same initial E- (solid lines) and B-mode (dashed lines) polarization with the different lensing potentials shown in Figure 4.1, presented as the percentage error $[1-(C^{XX}_{\ell,\mathrm{LensPix}}/C^{XX}_{\ell,\mathrm{Model}})]\times 100$ between the `CAMB` model and `LensPix`'s simulations. To compute these errors, `LensPix` C_ℓs were averaged over twenty five simulations.

Through these tests, we could not find a definite trend that allowed us to identify exactly where the error in the reproduction of lensed maps is coming from. Nevertheless, this accuracy problem would be further studied, because if not dealt with, it would limit delensing for the next generation of CMB maps. Some authors discuss that the explanation behind `LensPix` problems to accurately reproduce B-modes lies in the interpolation method used for remapping. Guilhem Lavaux and Benjamin Wandelt have designed an alternative interpolation technique that, based on the theory of isotropic Gaussian random fields, can provide optimal interpolated values for any field of arbitrary spin on the sphere [46]. They call this method *Fast and Lean Interpolation on the Sphere* (`FLINTS`[1]), and when applied to the production of lensed CMB maps, it is reported to produce maps two to three orders of magnitude more precise than `LensPix`. In particular, at the power spectrum level, lensing with `FLINTS` is said to be accurate to better than 0.5% at $\ell = 3000$ for temperature and both E- and B-mode polarization.

Having acknowledged `LensPix` issues with the simulation of B-mode polarization, we wanted to test whether such limitations were hindering the previously presented delensing fractions. For this purpose, we partially repeated the study done in section 3.1 using an alternative delensing technique known as *template delensing*. In template delensing, an estimation of the lensing potential and the observed lensed E-mode

[1] http://www2.iap.fr/users/lavaux/software/flints.html

map are used to produce a "template" of the expected B-mode polarization, which is then substracted from the observed B-mode map [27].

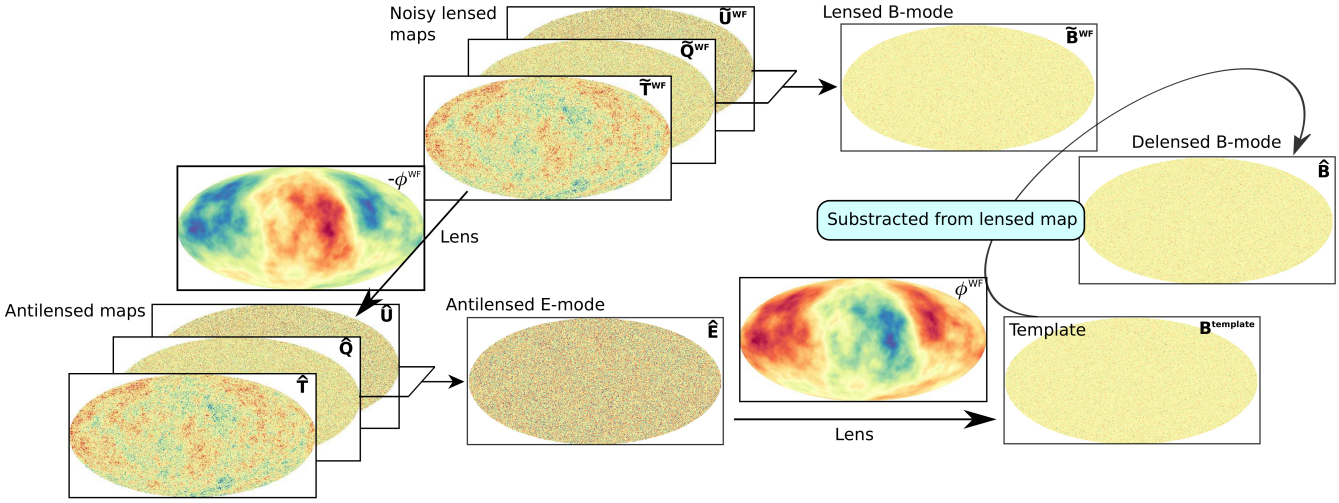

Figure 4.3: Flow diagram describing the template delensing pipeline. First, an estimation of the unlensed E-mode polarization is obtained from the previously antilensed Q and U maps. This E-mode map is then lensed to construct a template of the expected B-modes. Finally, the delensed B-mode map is calcuted by substracting that template from the initial lensed B-mode map.

To implement this new delensing process, we adopted the E-mode polarization map coming from the previously antilensed Q and U maps as the best estimation of the underlying unlensed E-mode. The B-mode template is then built by lensing the antilensed E-mode, and removed it from the lensed B-mode to produce the delensed map. When working with degraded CMB maps and limited lensing potential reconstructions, template delensing is said to achieve the same delensing efficiency than the remapping method [47]. However, its implementation in `LensPix` should report better results since now the lensing and antilensing operations are restricted to E-mode polarization, where `LensPix` is much more accurate, and B-modes only have to be simulated once, therefore reducing the accumulated numerical error.

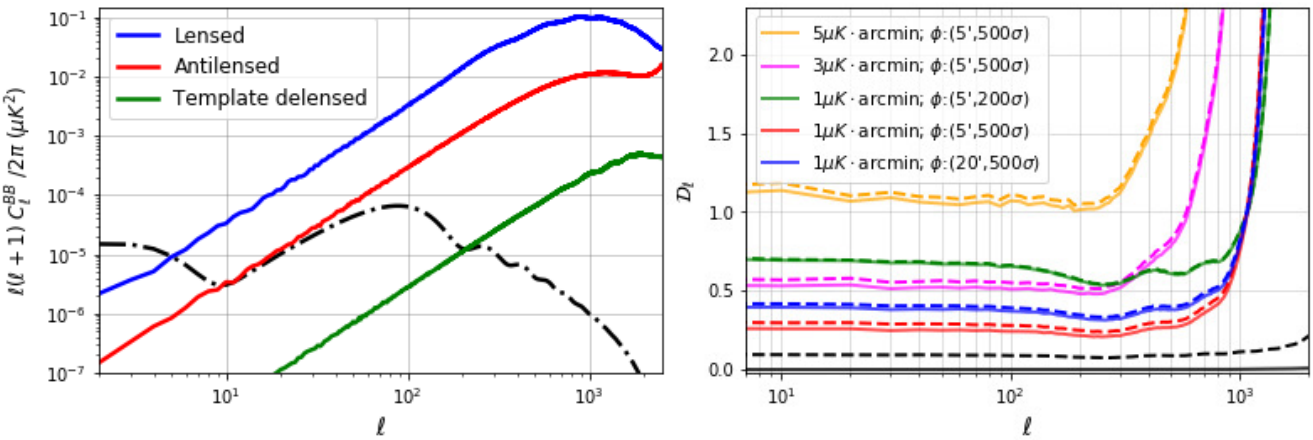

Figure 4.4: Comparison between the antilensing and template delensing techniques with `LensPix`. *Left panel:* In the ideal case where no noise or beam is added to either the CMB or lensing potential maps, template delensing proves to be up to two orders of magnitud better in the reduction of the lensed B-modes than the antilensing remapping. *Right panel:* Repetition of Figure 3.2, comparing this time the delensing fractions obtained with template delensing (solid lines) with their antilensing counterparts (dashed lines). Both cases correspond to a CMB map resolution of $\theta_{\mathrm{FWHM}} = 10'$.

As can be seen in the left panel of Figure 4.4, template delensing does prove to be up to two orders of magnitude better in the reduction of the lensed B-modes than the antilensing remapping for the ideal case where no noise or beam is added to either the CMB or the lensing potential map. In turn, this difference is

reduced when delensing is done with degraded maps (see right panel of Figure 4.4). Even in this case, template delensing fractions are still systematically better than their antilensing counterparts, although the difference between them is much smaller and seems to diminish as CMB and lensing potential maps are degraded. Figure 4.5 shows precisely the evolution of the relative difference between delensing techniques, $\Delta\mathcal{D}/\mathcal{D} = (\mathcal{D}_{antilensing} - \mathcal{D}_{template})/\mathcal{D}_{antilensing}$, as a function of the quality of lensing potential reconstructions.

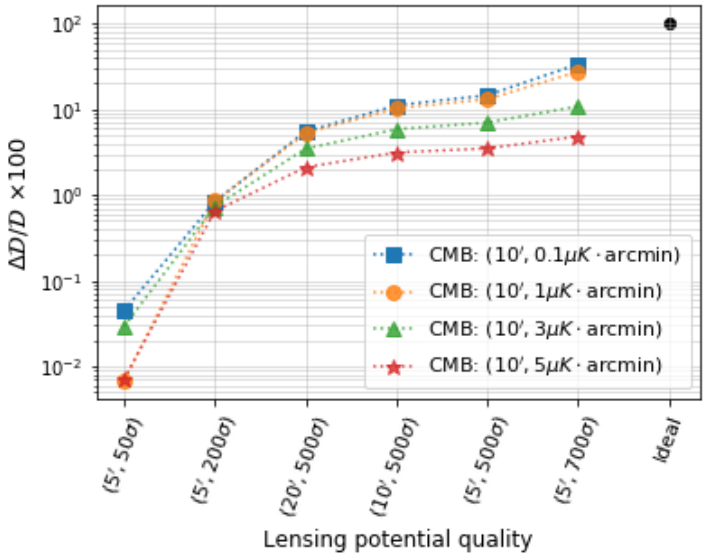

Figure 4.5: Relative difference between the delensing fractions obtained with antilensing and template delensing as the quality of CMB and lensing potential maps improves.

The fact that the use of template delensing, a method that works much better in the ideal case, stops reporting a significant benefit as map quality diminish demonstrates how map degradation is the dominant factor limiting delensing efficieny. Furthermore, the maximum absolute difference between delensing techniques is of $\Delta\mathcal{D} = 0.06$, hence delensing fractions from Table 3.1 are essentially correct and our results and subsequent discussion presented in chapter 3 are not limited by `LensPix` inaccuracies. Figure 4.5 also confirms how, in real-life situations, comparable delensing efficiencies are obtained through remapping and template delensing like affirmed by [47].

4.2 High-quality lensing potential reconstructions

Until now, lensing potential and CMB maps were completely detached: for every given CMB map, we assumed an external agent provided a map of the lensing potential that was used for delensing. However, since the lensing potential determines how the lensing kernel mixes and correlates the different scales, the resulting lensed CMB map contains enough information about the lensing potential to allow its reconstruction. Accordingly, we wanted to test whether the CMB maps from previous sections would be able to produce by themselves the high-quality 200σ and 500σ lensing potential reconstructions assumed in the delensing process.

For this, we employed *quadratic estimators*, one of the most extended techniques for lensing potential reconstruction. Since a detailed description of the formalism of quadratic estimators is way beyond the scope of this work, here we will settle for a brief commentary on how quadratic estimators exploit the

way lensing mixes the different multipoles to reconstruct the lensing potential. Nevertheless, a complete and thorough derivation can be found in [48]. The lensing kernel is known to correlate multipoles across a band determined by the power in the deflection angle $\nabla\phi$. When considering an ensemble average of CMB temperature and polarization fields lensed by the same ϕ, such correlation produces the addition of off-diagonal terms to the two-point correlation like

$$\langle \tilde{X}_{\ell m} \tilde{X}'_{\ell' m'} \rangle|_\phi = \tilde{C}_\ell^{XX'} \delta_{\ell\ell'} \delta_{m-m'} (-1)^m + \sum_{LM} (-1)^M \begin{pmatrix} \ell & \ell' & L \\ m & m' & -M \end{pmatrix} f_{\ell L \ell'}^{XX'} \phi_{LM}, \tag{4.1}$$

where $f_{\ell L \ell'}^{XX'}$ are the weights that dictate how unlensed multipoles are mixed for each pair of $X = T, E, B$ fields depending on their spin and parity. Therefore, these off-diagonal terms of the two-point correlation can be used to estimate the lensing potential. In a nutshell, that is exactly what quadratic estimators do:

$$\phi_{LM}^{XX'} = \frac{A_L^{XX'}}{L(L+1)} \sum_{\ell m} \sum_{\ell' m'} (-1)^M \begin{pmatrix} \ell & \ell' & L \\ m & m' & -M \end{pmatrix} g_{\ell\ell'}^{XX'}(L) \tilde{X}_{\ell m} \tilde{X}'_{\ell' m'}, \tag{4.2}$$

where $A_L^{XX'}$ is the appropiate normalization for each XX' combination. The new set of $g_{\ell L \ell'}^{XX'}$ weights controlling how multipoles are combined for each pair of fields are defined as those that minimize the variance of the estimatior. Through equation (4.2), five different estimators can be build to recover the lensing potential from a pair of CMB temperature and polarization maps: ϕ^{TT}, ϕ^{EE}, ϕ^{TE}, ϕ^{TB} and ϕ^{EB}. In principle, a sixth ϕ^{BB} is also possible, but in practice, B-mode polarization is too weak to produce a useful estimation by itself. Moreover, the correlations between these estimators can be further exploited to construct a minimum variance estimator (ϕ^{MV}) that improves the signal-to-noise of the reconstructed lensing potential.

Essentially, the lensing potential recovered with each $\phi^{XX'}$ estimator is just the true angular power spectrum of the lensing potential plus some reconstruction noise:

$$\langle \phi_{LM}^{XX'*} \phi_{L'M'}^{XX'} \rangle = \delta_{LL'} \delta_{MM'} [C_L^{\phi\phi} + N_L^{XX'}]. \tag{4.3}$$

In the framework of quadratic estimators, that reconstruction noise can also be calculated from the $A_L^{XX'}$ normalization, the $g_{\ell L \ell'}^{XX'}$ weights, and the lensed power spectrum of each pair or XX' fields. Once the reconstruction noise is known, it can be introduced in equation (2.6) to evaluate the quality of the reconstruction. Therefore, the $N_L^{XX'}$ power spectra is all we need to answer the question we posed at the beginning of this section.

We used the publicly avaible `quicklens` [2] code, a fast implementation of lensing estimators developed by Duncan Hanson, to calculate the $N_L^{XX'}$ power spectra of the lensing potential reconstruction that could be recovered from the CMB maps considered in previous sections. The `quicklens` package includes the full set of temperature and polarization estimators (ϕ^{TT}, ϕ^{EE}, ϕ^{TE}, ϕ^{TB} and ϕ^{EB}). From them, the minimum variance estimator had to be build following the recipe in [48]. Figure 4.6 shows an example of the reconstruction noise obtained when applying the quadratic and minimum variance estimators to CMB temperature and polarization maps with resolutions of $10'$ and $20'$, and noises of $5\mu K{\cdot}$arcmin and $1\mu K{\cdot}$arcmin.

[2] https://github.com/dhanson/quicklens

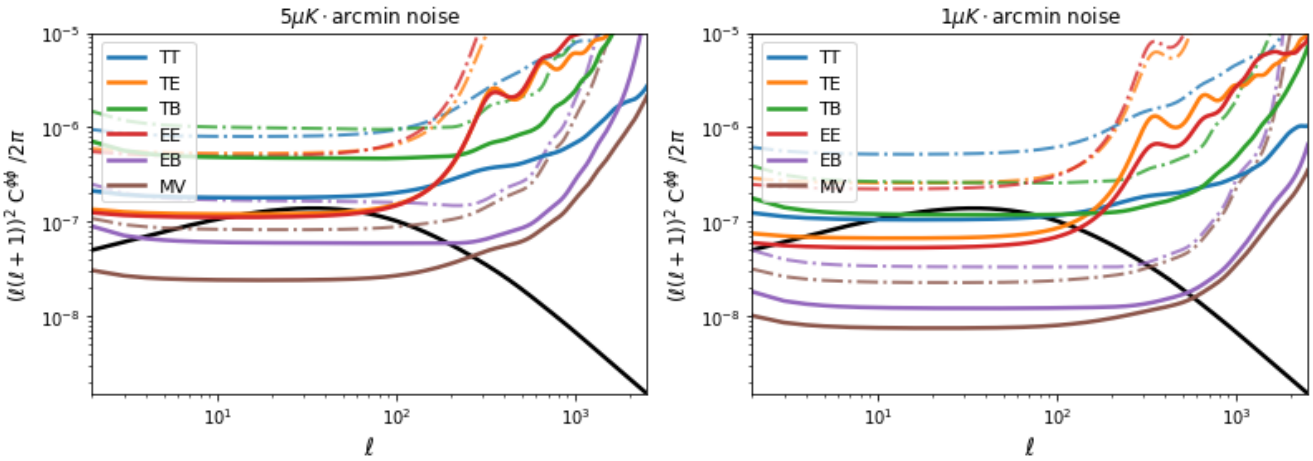

Figure 4.6: Lensing potential (black line) and noise power spectra obtained when applying the quadratic and minimum variance estimators to CMB temperature and polarization maps with different resolutions and levels of instrumental noise. The solid lines correspond to CMB maps with a $10'$ resolution, and the dot-dashed ones to a resolution of $20'$. The reconstruction noise associated to each estimator was computed using the `quicklens` code.

As can be seen in this figure, there is a clear hierarchy amongst estimators. Polarization maps provide a more direct probe of the lensing potential than temperature ones [49], hence resulting in lower reconstruction noises. In this way, the best reconstruction is produced by the ϕ^{EB} estimator, only surpassed by the minimim variance estimator. It is also worth noting how these noise spectra have a much more complex structure than the simple constant N_ℓ we assumed for our simulations. One may think this should affect the delensing process, specially at large scales where $N_L^{XX'}$ has an important component while our noise is negligible. However, since we work with Wiener filtered lensing potential maps, that is not the case. Noise spectra from the minimum variance estimator are low enough compared with the true lensing potential spectrum at large scales that the Wiener filter is able to succesfully recover the underlying lensing potential.

	$\theta_{\rm FWHM} = 10'$		$\theta_{\rm FWHM} = 20'$	
σ_n /μK·arcmin	σ_ϕ	$\mathcal{D}$	σ_ϕ	$\mathcal{D}$
5	176	-	91	-
3	234	0.75	130	0.85
1	344	0.48	204	0.65
0.1	506	0.30	299	0.51
0	663	0.18	663	0.18

Table 4.1: Estimation of the quality of the lensing potential reconstructions that a minimum variance estimator could produce from the CMB maps considered in previous sections. Using the simple laws we fitted in section 3.1, we can also predict the delensing fraction associated to such combination of CMB map and lensing potential. The last row indicates the best lensing reconstruction possible from such CMB maps up to $\ell_{max} = 2500$.

Finally, Table 4.1 containts the number of σs of the lensing potential reconstruction that the miminum variance estimator was able to produce from the CMB maps considered in previous sections. Thanks to the $a\sigma_\phi^n + b$ law we fitted in section 3.1, we can also predict the delensing fraction that could be produced with such reconstructions. These results tell us how, indeed, it is possible to recover the previously assumed 200σ and 500σ reconstructions from CMB maps of a $10'$ resolution. The relation between the noise of the CMB map and the quality of the reconstruction can be fitted by an $a\sigma_n^m + b$ power law, allowing us to predict that for $10'$ resolution maps a 200σ reconstruction will be possible for a $3.87\mu K$·arcmin noise level, and that a 500σ reconstruction will need a $0.12\mu K$·arcmin noise (see Figure 4.7). However noises below the $1\mu K$·arcmin level would not be achieved by any full-sky mission in the near future. Ground missions may be able to reach that noise level, but only for small regions of the sky. Another noteworthy feature is that, although the resolution of CMB maps was not a very relevant factor for delensing, it does

play a very important role in the internal reconstruction of the lensing potential. For the same noise level, reconstructions coming from $10'$ resolution maps can reach signal-to-noise ratios hundreds of σs higher than those coming from $20'$ resolution maps.

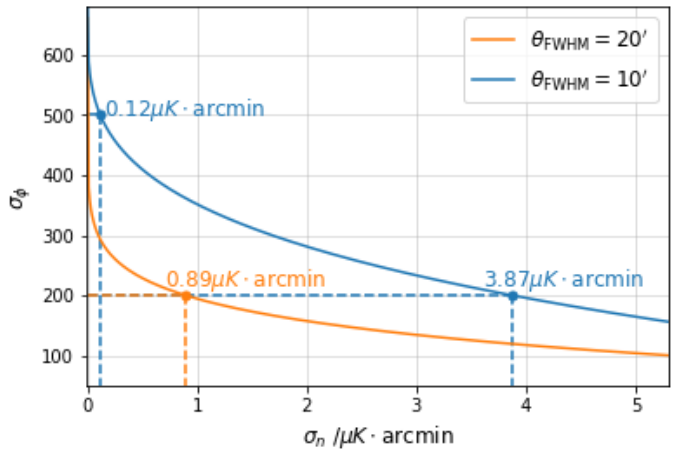

Figure 4.7: Fitting the dependence between quality of the lensing potential reconstruction and CMB map noise with an $a\sigma_n^m + b$ power law we can predict that for $10'$ resolution maps, a 200σ reconstruction will be possible for a $3.87\mu K\cdot$arcmin noise level, and that a 500σ reconstruction will need a $0.12\mu K\cdot$arcmin noise.

As a final remark, the last row of Table 4.1 shows the best lensing reconstruction that minimum variance estimators can produce from CMB tempature and polarization maps up to $\ell_{max} = 2500$. To go beyond that limit, and in general to improve the signal-to-noise ratio of all reconstructions, other techniques must be used. In fact, although quadratic estimators have been successfully employed to recover the lensing potential from *Planck* data in the past [33], their performance is known to be suboptimal at the noise levels expected from future experiments, especially for polarization, and more sophisticated techniques are being developed [36, 50].

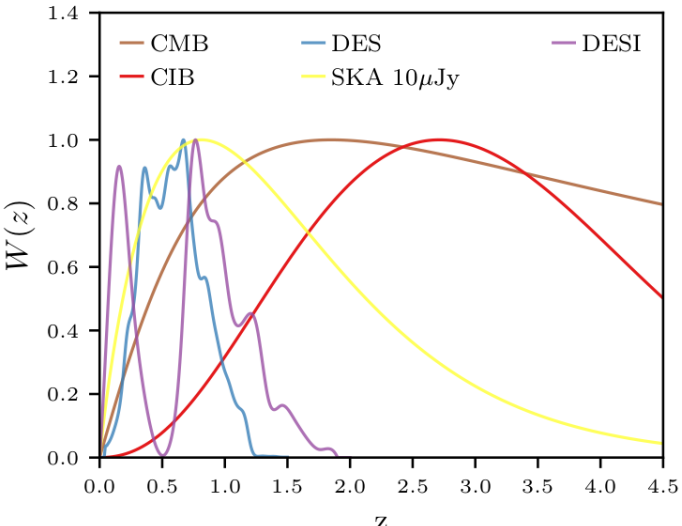

Figure 4.8: Comparison of the lensing kernels of different large-scale structure tracers. As a rule of thumb, the larger the overlap with the CMB lensing kernel the better the reconstruction of the lensing potential. Figure taken from [34].

As a complementary approach, the lensing potential can also be recovered from other large-scale structure tracers, like galaxy surveys [51], the Cosmic Infrared Background (CIB) [52, 53], or tomographic line intensity mapping [54, 55]. Through these tracers lensing potential reconstructions are not as straightforward, since structure at different redshifts contributes differently to the generation of B-modes because of the geometric properties of the lensing kernel (see Figure 4.8) [34]. In this way, different tracers can

be used to improve lensing potential reconstrucionts at different scales [56]. However, it must be noted that these emissions come from cosmological distances, and therefore they are also lensed. When not accounted for, these additional lensed signals are known to introduce biases in internal CMB lensing reconstructions [57]. The CIB, a diffuse infrared radiation generated by star-forming galaxies, has been the most extended tracer in recent years due to its great correlation with the CMB. As an example, it has already been succesfully used by the SPTPol [58] and Planck Collaborations [27] to increase the signal-to-noise of their lensing maps at small scales.

CHAPTER 5

Conclusions and future work

In this work, we found a $5\mu K$·arcmin white noise to be the natural limit for delensing, meaning that for CMB maps with that level of noise no delensing effort managed to reduced the lensed B-mode. For delensing to become successful, CMB maps should have an instrumental noise below $\sigma_n = 4.5\mu K$·arcmin. Conversely, the resolution of the CMB map is not a strong conditioner for delensing efficiency. Besides a low level of noise, the main requirement to achieve a good delensing is to have a good estimation of the lensing potential. In order to reduce lensed B-modes to half their power, at least 500σ reconstructions are needed. Currently, full-sky lensing potential reconstructions are far from reaching such quality (the *Planck* mission only obtained a 40σ reconstruction [27]), but much better reconstructions could be produced from the polarization maps coming from the next generation of CMB experiments. To internally produce such high-quality reconstructions is when a high CMB map resolution becomes crucial. Additionally, lensing potential reconstructions can be improved by combining CMB polarization with other large-scale tracers.

For our discussion, we considered an ideal CMB map where only the instrumental noise and resolution limited the quality of the internal lensing potential reconstruction. However, the remaining contribution from microwave foregrounds will also be an obstacle when attempting to recover the lensing potential from real-life CMB temperature and polarization maps. In particular, given how sensitive to map resolution internal reconstructions proved to be, extragalactic point-like sources may result very harmful since they dominate the smallest scales. In this way, more faithfull predictions on the quality of lensing potential reconstructions would be obtained if a residual foreground component was also taken into account. Therefore, understanding how foregrounds affect lensing potential reconstructions, and to what extent could they limit future experiments, will be a topic of future study.

Although we proved that delensing always improves the chances at detection, the signal-to-noise ratios associated to a primordial B-mode are still low for tensor-to-scalar ratios $r \leq 1 \times 10^{-3}$ when the contribution of galactic foregrounds is also considered. It is only in the optimistic scenario of a $1\mu K$·arcmin noise and a delensing fraction of $\mathcal{D} < 0.55$ that the signal-to-noise ratio is expected to rise above the $S/N = 5$ threshold for $r = 1 \times 10^{-3}$. We predict that, after marginalizing over the foreground contribution, an almost 2σ detection of an $r = 6 \times 10^{-4}$ primordial B-mode could be made from CMB maps with noises of $3\mu K$·arcmin and $1\mu K$·arcmin if delensing fractions of, respectively, $\mathcal{D} = 0.56$ and $\mathcal{D} = 0.68$ could be met. We found a reduction of the instrumental noise of CMB maps to be the most effective action to improve the signal-to-noise ratio since it reduces the cosmic variance and boosts

delensing efficiency at the same time.

In addition, the detection of a primordial B-mode would also benefit from a combined analysis of data from satellite and ground-based missions. Each of this opposite experimental settings has different advantages to offer: satellite missions have full-sky coverage, granting access to the largest scales and a better sampling variance; while ground-based experiments are restricted to a small region of the sky, but allow for better instrumental noises and resolutions. When fitting different components into the observed angular power spectrum (like it was done in section 3.2), it is easy to identify, and hence replace, the contribution that each multipole has on the overall likelihood function. In this way, a combined likelihood function could be built to exploit the best features of both settings. A joint analysis like this one is already being considered for the future LiteBIRD and Stage-IV experiments.

We also discovered that the `LensPix` code does not have the same accuracy in the reproduction of lensed B-modes than for temperature and E-mode polarization, which will limit the delensing operation for the next generation of CMB maps. From the tests we ran, we could not find a definite trend that allowed us to identify the cause of that inaccuracy. Nevertheless, it will be a topic of further study. A task left pending in this work was to check whether the better interpolation of the `FLINTS` code does indeed make up for the shortcomings of `LensPix` when it comes to the simulation of lensed B-modes. If that was not the case, then a more precise code would need to be designed.

Finally, after this comprehensive study of the delensing process, we are now ready to apply the acquired knowledge and tools to forecasts the viability of delensing, and the benefits it would report in regards to primordial B-mode detection, for specific future CMB experiments like the already approved JAXA's LiteBIRD satellite or the PICO satellite proposed by NASA.

Bibliography

[1] LIGO Scientific Collaboration and Virgo Collaboration *Phys. Rev. Lett.* **116**, 061102 (2016)

[2] LIGO Scientific Collaboration and Virgo Collaboration. *GraceDB — Gravitational Wave Candidate Event Database*. https://gracedb.ligo.org/superevents/public/O3/

[3] Pitkin, M. *et al. Living Rev. Relativ.*, **14**:5 (2011)

[4] Caprini, C. and Figueroa, D. G. *Class. Quantum Gravity* **35**, 163001 (2018)

[5] Flanagan, É. É. and Hughes, S. A. *New J. Phys.* **7** 204 (2005)

[6] Bishop, N. T. and Rezzolla, L. *Living Rev. Relativ.*, **19**:2 (2016)

[7] Baumann, D. *Lectures on Cosmology*. Cosmology course at Cambridge's DAMTP. Available at: http://theory.uchicago.edu/~liantaow/my-teaching/dark-matter-472/lectures.pdf

[8] Planck Collaboration I *arXiv astrophysics e-prints* arXiv:1807.06205 [astro-ph.CO] (2018)

[9] Guth, A. H. *Phys. Rev. D* **23**, 347 (1981)

[10] Baumann, D. *arXiv astrophysics e-prints* arXiv:0907.5424v2 [hep-th] (2009)

[11] Grishchuk, L. P. *Soviet Physics JETP* **40**, p.409 (1975)

[12] Starobinsky, A. A. *Soviet JETP Letters* **30**, p. 682 (1979)

[13] Watanabe, Y. and Komatsu, E. *Phys. Rev. D* **73**, 123515 (2006)

[14] Samtleben, D., Staggs, S. and Winstein, B. *Annu. Rev. Nucl. Part. Sci.* 57:1, 245-283 (2007)

[15] Fixsen, D. J. *ApJ*, **707**(2) (2009)

[16] Hu, W. and White, M. *New Astron.* **2**(4) p. 323 (1997)

[17] Rybicki, G. B. and Lightman, A. P. (1985). *Radiative Processes in Astrophysics*. WILEY-VCH Verlag GmbH & Co. KGaA. ISBN:9780471827597

[18] Cabella, P. and Kamionkowski, M. *arXiv astrophysics e-prints* arXiv:1305.5422 [astro-ph] (2004)

[19] Kamionkowski, M. and Kovetz, E. D. *Annu. Rev. Astron. Astrophys*, **54**:227-269 (2016)

[20] Polnarev, A. G. *SvA*, **29**, p. 607 (1985)

[21] Zhao, W. and Zhang, Y. *Phys. Rev. D* **74**, 083006 (2006)

[22] Kamionkowski, M., Kosowsky, A. and Stebbins, A. *Phys. Rev. Lett.* **78**, 2058. (1997)

[23] Dickinson, C. *arXiv astrophysics e-prints* arXiv:1606.03606 [astro-ph.CO] (2016)

[24] BICEP2 Collaboration *Phys. Rev. Lett.* **112**, 241101 (2014)

[25] BICEP2/Keck and Planck Collaborations *Phys. Rev. Lett.* **114**, 101301 (2015)

[26] Lewis, A. and Challinor, A. *Phys. Rept.* **429**, 1 (2006)

[27] Planck Collaboration VIII *arXiv astrophysics e-prints* arXiv:1807.06210 [astro-ph.CO] (2018)

[28] Planck Collaboration VI *arXiv astrophysics e-prints* arXiv:1807.06209 [astro-ph.CO] (2018)

[29] Hu, W. *Phys. Rev. D* **62**, 043007 (2000)

[30] Lewis, A. *Phys. Rev. D* **71**, 083008 (2005)

[31] Gorski, K. *et al. arXiv astrophysics e-prints* arXiv:astro-ph/9905275 (1999)

[32] Akima, H. *ACM TOMS* **22**(3), p. 362 (1996)

[33] Carron, J., Lewis, A. and Challinor, A. *JCAP* (2017)035

[34] Manzotti, A. *Phys. Rev. D* **97**, 043527 (2018)

[35] Anderes, E., Wandelt, B. D. and Lavaux, G. *ApJ*, **808**(2) (2015)

[36] Carron, J. and Lewis, A. *Phys. Rev. D* **96**, 063510 (2017)

[37] Planck Collaboration VIII *A& A* 594, A8 (2016)

[38] Hazumi, M. *et al. J. Low Temp. Phys* **194**(5-6), 443-452 (2019)

[39] Abazajian, K. N. *et al. arXiv astrophysics e-prints* arXiv:1610.02743 [astro-ph.CO] (2016)

[40] Elsner, F. and Wandelt, B. D. *arXiv astrophysics e-prints* arXiv:1211.0585 [astro-ph.CO] (2012)

[41] Barreiro, R. B. *et al. IEEE J-STSP* **2**(5), p. 747 (2008)

[42] Caldeira, J. *et al. Astron. Comput.* **28**, 100307 (2019)

[43] Errard, J. *et al. JCAP* (2016)052

[44] Ly, A. *et al. arXiv astrophysics e-prints* arXiv:1705.01064 [math.ST] (2017)

[45] Coe, D. *arXiv astrophysics e-prints* arXiv:0906.4123 [astro-ph.IM] (2009)

[46] Lavaux, G. and Wandelt, B. D. *ApJS*, **191**(1) (2010)

[47] Namikawa, T. *Phys. Rev. D* **95**, 103514 (2017)

[48] Okamoto, T. and Hu, W. *Phys. Rev. D* **67**, 083002 (2003)

[49] Hu, W and Okamoto, T. *ApJ*, **574**(2) (2002)

[50] Hadzhiyska, B. *et al. Phys. Rev. D* **100**, 023547 (2019)

[51] Namikawa, T. *et al. Phys. Rev. D* **93**, 043527 (2016)

[52] Sherwin, B. D. and Schmittfull, M. *Phys. Rev. D* **92**, 043005 (2015)

[53] Larsen, P. *et al. Phys. Rev. Lett.* **117**, 151102 (2016)

[54] Kovetz, E. D. *et al. arXiv astrophysics e-prints* arXiv:1709.09066 [astro-ph.CO] (2017)

[55] Karkare, K. S. *arXiv astrophysics e-prints* arXiv:1908.08128 [astro-ph.CO] (2019)

[56] Yu, B., Hill, J. C. and Sherwin, B. D. *Phys. Rev. D* **96**, 123511 (2017)

[57] Mishra, N. and Schaan, E. *arXiv astrophysics e-prints* arXiv:1908.08057 [astro-ph.CO] (2019)

[58] SPTPol Collaboration *ApJ*, **846**(1) (2017)